

國立交通大學

電子工程系

碩士論文

異常光學穿透現象於兆赫波段之研究

Study of Extraordinary Optical Transmission in THz Region

研究生：黃品維

指導教授：李建平 教授

中華民國九十八年六月

異常光學穿透現象於兆赫波段之研究

Study of Extraordinary Optical Transmission in THz Region

研究生：黃品維

Student : Pin-Wei Huang

指導教授：李建平

Advisor : Chien-Ping Lee

國立交通大學

電子工程系

碩士論文

A Thesis

Submitted to Department of Electronic Engineering
College of Electrical Engineering and Computer Science

National Chiao Tung University

in partial Fulfillment of the Requirements

for the Degree of

Master

in

Electronic Engineering

June 2009

Hsinchu, Taiwan, Republic of China

中華民國九十八年六月

異常光學穿透現象於兆赫波段之研究

學生：黃品維

指導教授：李建平 博士

國立交通大學

電子工程學系 電子研究所碩士班

摘要

本論文針對近年來相當熱門的一個研究主題—異常光學穿透 (EOT) 現象—在兆赫波段上進行深入的物理探討。目前已知的是在金屬上週期性排列的孔洞會造成 EOT，但此現象的物理機制仍在爭論中，而在 THz 波段，一些導電性好金屬可視為完美導體，因此表面電漿子理論在此波段的解釋並不適當。

第一個部分為理論推導，我們將整個系統的電磁場做模態展開，此電磁場滿足馬克斯威爾方程式及其所推演出的荷姆霍茲方程式，計算的結果與實驗結果十分穩合。此結果排除了表面電漿子理論在此波段的解釋。

第二個部分我們探討孔洞的形狀大小對穿透頻譜的影響。結果顯示：1) 孔洞的面積愈小絕對穿透效率愈高，2) 孔洞的寬長比會對頻譜造成非單調的紅移現象，3) 孔洞和晶格的對稱性關係亦會對頻譜造成顯著的影響，這些特性可以為日後的兆赫波微光學元件應用提供一個新的指引。

Study of Extraordinary Optical Transmission in THz Region

Student: Pin-Wei Huang

Advisor: Dr. Chien-Ping Lee

Department of Electronics Engineering & Institute of Electronics

National Chiao Tung University

Abstract

This thesis studies the physical origin of a very popular research theme, extraordinary optical transmission (EOT) phenomenon, in THz region. It is known that 2D periodic metal hole arrays can cause EOT; however, the real physical mechanism of this phenomenon is under debate. In THz region, good conductors can be seen as perfect electric conductor and therefore the explanation based on theory of surface plasmon polariton (SPP) is improper.

The first part of this thesis is theoretical formalism. We expand the EM fields of the system by eigenfunctions of Helmholtz's equations in each sub-system, and then match the boundary condition obeying Maxwell's equations. The simulation results match very well with experiment results, and so that we can exclude the SPP effect in THz region.

In the second part we investigate the influence of hole shape and size on transmission spectrum. It is shown that, 1) the smaller the hole area, the higher the absolute transmission efficiency, 2) the aspect ratio of holes can cause shift in the peak transmission spectrum non-monotonously, and 3) the symmetry difference between hole and unit cell also has influence on transmission spectrum. These properties can be taken as a guide for future micro-optic THz device.

Acknowledgement (誌謝)

今年是我在交大的第六個年頭，六年看似不算短的時間，但對我而言真的是時光飛逝。大學在電工系四年就已讓我眼界大開，而最後兩年的碩士生涯讓我進步的最多，讓我更清楚自己的所學不足，讓我更加確認自己必須加強學理基礎以繼續邁向未來的研究生涯。首先我必須感謝我的指導教授 李建平 博士及 顏順通 博士，他們二位在這兩年提供我一個自由且資源豐富的研究環境，以及每每在私底下或會議中認真且嚴謹的指導及討論。每次討論後我都感受到科學的洗禮，並且在邏輯觀念的思考上更加成熟。另外我必須感謝 鐘佩鋼 學長，沒有他在 FTIR 量測上無私地幫忙及指導，我是不可能如期完成這次的碩士論文，於此再次感謝 鐘佩鋼 學長。接下來我要感謝 謝泓文 學弟在計算上的協助、王德賢 學長在許多物理觀念上的糾正，及研究伙伴 賴威良、黃信傑 有關於實驗方法與研究上的討論，我常花費他們許多寶貴的時間。接下來我要感謝所有 MBE Lab 的教授們、學長們及同學們，他們時常也是提供我許多必要的協助及討論。再來就是感謝電工九六級的許多同學們，在我曾經極度低潮時，陪伴我、鼓勵我，使我更加感受到交大與其他大學不一樣的地方—同儕間的革命情感。最後，我要感謝我的父母和兄姊，感謝他們這二十五個年頭的照顧，使我可以擁有一個圓滿的家庭而無後顧之憂地求學，還有 Jerry 姊夫在許多生活上及升學上的幫忙，當然還要感謝我的愛犬—哈利，牠也是陪我渡過了十七個年頭，常常讓我忘卻許多煩惱，感謝老天讓牠可以陪我從小學走到目前碩士這個階段，謝謝老天爺!

品維

2009 夏于風城

Contents

Chinese Abstract (摘要)	i
English Abstract	ii
Acknowledgement (誌謝)	iii
Contents	iv
List of Figures	vi
Chapter 1 Introduction	1
1.1 Diffraction Theory of Gratings	1
1.2 Wood's Anomalies	2
1.3 Surface Plasmon Polaritons	4
1.4 Extraordinary Optical Transmission Through Sub-Wavelength Metallic Hole Arrays	4
1.5 Spoof Surface Plasmon	7
Chapter 2 Measurement Method	8
Chapter 3 Sample Design and Fabrication	12
Chapter 4 Theoretical Formalism	19
Chapter 5 Simulation Results and Discussions	30
5.1 Preamble	30
5.2 Simulation Results Compared with Measurement Results: EOT Phenomenon	32

5.3 Simulation Results Compared with Measurement Results:	
Non-Monotonous Red-Shift Phenomenon-----	37
5.4 Simulation Results Compared with Measurement Results:	
Symmetry Effect -----	47
Chapter 6 Conclusion -----	55
Bibliography-----	56
Autobiography (自傳)-----	58



List of Figures

Fig. 1.1	The schematic description of diffraction process-----	3
Fig. 1.2	Zero-order transmission spectrum of hoe array on Ag-----	6
Fig. 2.1	Schematics of a Michelson interferometer -----	9
Fig. 2.2	Examples of spectra and their corresponding interferograms -----	11
Fig. 2.3	Three kinds of transmission spectra-----	11
Fig. 3.1	(a) Top-view of the sample under measurement. (b) Side-view of the sample under measurement-----	14
Fig. 3.2	Transmission spectra with various aspect ratios -----	15
Fig. 3.3	Transmission spectra with various aspect ratios-----	16
Fig. 3.4	Transmission spectra with same aspect ratios-----	16
Fig. 3.5	(a) (b) Transmission spectra with symmetry effect-----	17
	(c) (d) Transmission spectra with symmetry effect-----	18
Fig. 4.1	(a) Top view of unit cell of rectangular lattice -----	22
	(b) Schematics of the system under study-----	22
	(c) Schematics of the system with incident light-----	22
Fig. 5.1	Comparison between measured and simulated transmission spectra -----	34
Fig. 5.2	The absolute transmission efficiency-----	34
Fig. 5.3	Energy potential of resonant tunneling-----	35
Fig. 5.4	Transmittance spectrum for free standing 2D metal hole array-----	35
Fig. 5.5	Transmission spectrum of for resonant tunneling-----	36
Fig. 5.6	(a) (b) Evolution of transmission spectra-----	40
	(c) (d) Evolution of transmission spectra-----	41
Fig. 5.7	Evolution of transmission spectra-----	43
Fig.5.8	(a) The transmission of resonant tunneling with narrower barriers (b) The transmission of resonant tunneling with wider barriers -----	44
Fig. 5.9	Polarization dependence-----	45
Fig.5.10	Weak coupling strength between waveguide and plane mode-----	45
Fig. 5.11	Decoupling of the periodicity resonance and hole resonance -----	46
Fig. 5.12	(a) (b) Evolution of transmission spectra -----	49
Fig. 5.13	(a) (b) Evolution of transmission spectra-----	50
	(c) Evolution of transmission spectra with higher resolution-----	51
Fig. 5.14	(a) (b) Symmetry effect: evolution of transmission spectra-----	52
Fig. 5.15	(a) (b) Symmetry effect: evolution of transmission spectra-----	53
Fig. 5.16	(a) The general structure of PC for calculation of FDM-----	54
	(b) The eigenfrequency distribution of two dielectric photonic crystals with different structures-----	54

Chapter 1 Introduction

Terahertz (THz) radiation lies between 0.1-10 THz in frequency region or 3mm-30 μm in wavelength region or 3 cm^{-1} - 300 cm^{-1} in wavenumber region. The region is between the microwave and infrared portion of the electromagnetic spectrum. Most materials in Nature don't have a useful electronic and/or photonic response in THz region. This results in hard challenges in the creation of the devices for generation, filter and detection of THz wave. This is the well-known "THz gap". However, researchers never stop looking for novel THz devices in order to take advantages of THz region. The promising advantages include sensing, communication, and imaging. Therefore, our goal of this study is to utilize an ordinary material (say, metal) with ordinary structure (say, periodic array) to achieve extraordinary effect in THz region. In this thesis we will focus on how a periodic structure interacts with THz wave.

1.1 Diffraction Theory of Gratings

Theory of diffraction grating can be traced back to the beginning of 19th century when T. Young and J. Fraunhofer made the first optical diffraction gratings and revealed the role of optical diffraction in their behavior. The scattering behaviors of diffraction gratings can be described basically by the conservation law of wave momentum such as $\mathbf{k}_{\text{scatt}} = \mathbf{k}_{\text{inc}} + \mathbf{G}$, where $\mathbf{k}_{\text{scatt}}$, \mathbf{k}_{inc} are the momentums of scattered and incident wave momentum respectively, and \mathbf{G} is the reciprocal lattice vector of the grating such that $\mathbf{G} \cdot \mathbf{a} = 2\pi m$, where \mathbf{a} is the basis vector of the lattice in real space and m is an arbitrary integer. For example, **Fig. 1.1** depicts a

reflecting grating showing an incident wave being scattered by the grating into three orders, $m = 0$, $m = 1$, and $m = -1$. The idea of diffraction on grating didn't be challenged until Ebbesen's findings [1]. Up to our best knowledge, before Ebbesen's experiment, all studies had focused on the transmission of band-pass metal hole arrays occurring in the region, $d < \lambda < \lambda_c$, where d is the lattice constant of the arrays, λ_c is the cut-off wavelength for electromagnetic modes inside the holes, and λ is the incoming wavelength. The long wavelength filtering is due to the cutoff by the holes, and the short wavelength filtering is due to occurring of energy redistribution when the first diffraction mode becomes propagating. However, Ebbesen found an unexpected transmission spectra in the regime, $\lambda_c < d < \lambda$. Thus there must be a different mechanism responsible for this unexpected transmission spectra and promoted a study resurgence of such grating structures.

1.2 Wood's Anomalies

“Wood's anomalies” is observed by R. W. Wood, who discovered some unexpected patterns in the spectrum of light resolved by optical diffraction gratings, in 1902 [2]. Later than Wood's discovery, Rayleigh and U. Fano explained the phenomenon respectively [3][4]. It is explained by Rayleigh that the energy of diffracted wave can be redistributed at specific diffracted orders. For instance, considering the case of **Fig. 1.1**, we note that the diffracted order, $m = 1$ in the figure, becomes tangent to the grating surface just before its vanishing. In this case, the normal momentum k_z of diffracted wave becomes imaginary right after being zero. Then the order ($m = 1$) becomes evanescent in the direction of OZ axis. The energy of this order will be redistributed to other orders not satisfying the condition,

$\sqrt{k_0^2 - |\mathbf{k}_{0//} + \mathbf{G}|^2} = 0$ and then be reflected. Therefore, there will be minima at the transmission spectrum. We call it “Rayleigh’s anomaly”, and the wavelengths at which the minima occur are called “Rayleigh’s wavelengths”. Explanation to the peak of the spectrum is first proposed by U. Fano around 1938. He related the anomalies (peak) to a resonance effect. The resonances arise from the coupling between a discrete eigenmode of the grating and continuous diffraction modes. They occur right after the Rayleigh wavelengths. We call it “resonant anomalies”, or “Fano’s anomalies”.

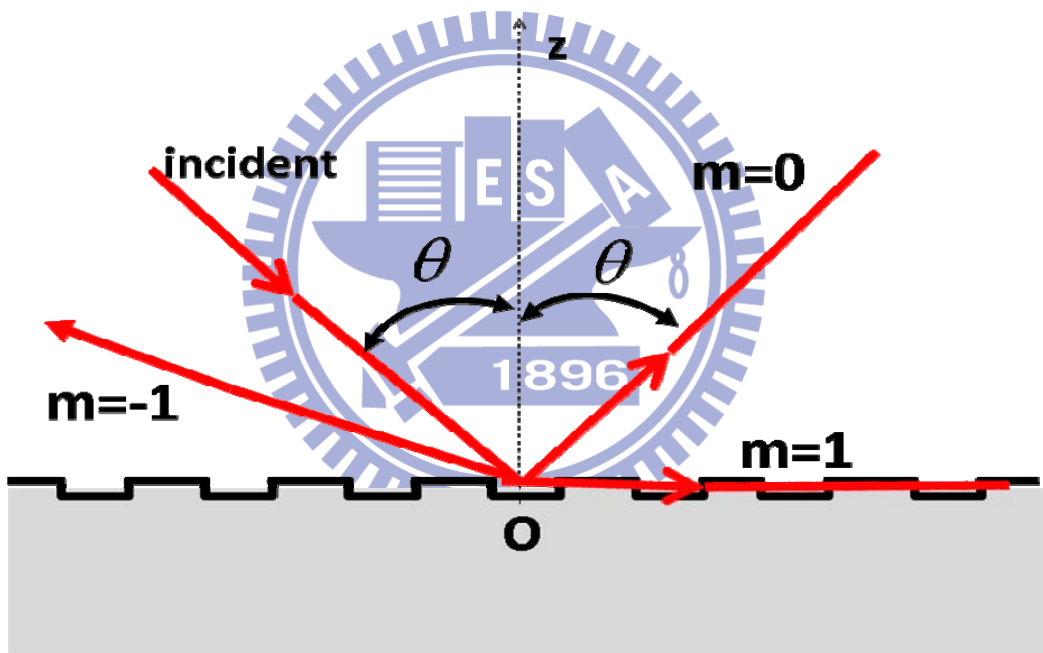


Fig. 1.1 The schematic description of the process of diffraction. “m” is the diffraction order.

1.3 Surface Plasmon Polaritons

Surface plasmon is a surface wave due to collective oscillation of carriers (electrons) in conducting materials such as metals or doped semiconductors at optical frequency [5]. This surface mode is confined at the interface between materials with positive and negative dielectric constants respectively. Furthermore, if electromagnetic wave is coupled with the carriers at the surface, we call it surface plasmon polariton (SPP). To get a simple physical picture, we can consider the following situation: a stimulating electric field creates two opposite electric displacements in phase with each other across the interface. From Maxwell's equations, we can see that these two opposite displacements act to attract and confine an AC current to the interface, and thus generate the collective oscillation of electrons. The mathematical description of the phenomenon of SPP can be referred to Ref. [5]. Then a dispersion relation of this non-radiative electromagnetic mode can be derived. We don't derive the dispersion relation here because in fact it is not the mechanism responsible for the phenomenon in our system.

1.4 Extraordinary Optical Transmission (EOT) through Sub-Wavelength

Metallic Hole Arrays

In 1998, Ebbesen et al. reported the surprising property of optical transmission on metallic gratings [1]. They drilled cylindrical holes (150nm for the diameter) in optically thick (200nm) metallic films in fashion of 2D lattice (900nm for the lattice constant) on a glass. Although bi-dimensional metallic gratings have been studied over many years before 1998, the most attractive characteristic of their findings was the distinct spectrum of transmission, as shown in the **Fig. 1.2**. In **Fig. 1.2**, the peculiar part of the spectrum is the transmission intensity at the wavelengths above

the periodicity, a_0 . We have already known that the minimum at a_0 is the result of Rayleigh type of Wood's anomalies, and the peak right after a_0 can, in general, be explained by the Fano type. However, the peculiarity is that another peak occurs at even longer wavelength (1370nm) which is nearly ten times the hole diameter. Furthermore, if focusing on the transmission efficiency, one can find that the absolute transmission efficiency obtained by taking the ratio of total transmittance (zero-order) to the fraction of surface area occupied by the holes is larger than 2. That is, more than twice as much as energy can be transmitted through the holes when the light illuminates directly on hole area. This new phenomenon cannot be explained by Bethe's theory which states that the transmission efficiency of a single sub-wavelength aperture can be described as $(r/\lambda)^4$ [6]. Apparently, the existence of grating does change the whole situation. Ebbesen attributed this phenomenon to the resonant excitation of surface plasmon polaritons (SPP). After Ebbesen, many researchers backed up this explanation by investigating this SPP-enhanced phenomenon both theoretically [7] [8] and experimentally [9]. However, there are other researchers questioning this SPP explanation. Theoretically they found that even a structure such as perfect electrical conductor (PEC) which cannot support surface plasmon on it also has a bounded surface wave on its surface [10][11], and hence can cause an extraordinary optical transmission [12]. Additionally, even both matter waves [13] and sound waves [14][15] through holey slabs show extraordinary transmission phenomenon.

In this thesis, we focus on the EOT phenomenon with nearly perfect electrical conductor (PEC). In fact, no PEC exists in real world. However, our experiments were conducted in the THz region and for some highly conducting metals, Ag, Au and Al,

the skin depths of those metals can be calculated to be several tens of nanometers, and can be negligible when compared to the incident wavelength.

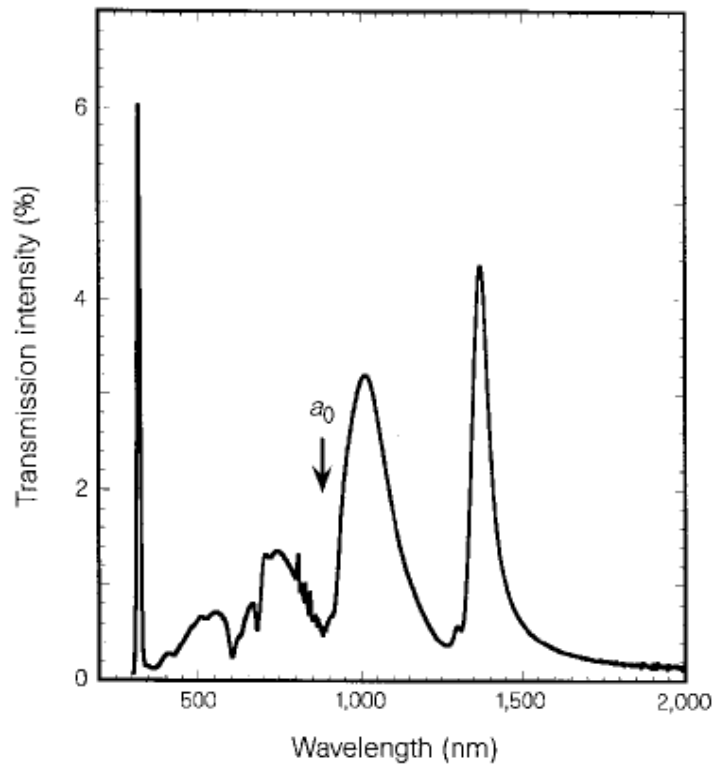


Fig. 1.2 Zero-order transmission spectrum of hoe array on Ag [1].

1.5 Spoof Surface Plasmon

In 2004, J. B. Pendry, et al. reported an original work showing that even a perfect conductor can support confined surface wave as long as the surface are not purely flat [10]. The authors call this surface mode “Spoof Surface Plasmon”. Because such spoof surface plasmon (SSP) involves no carriers in the metal, they concluded that it is simply the geometry of the structure responsible for this surface mode. They also suggested that there will be a hybrid surface mode, which is the mixture of surface plasmon and spoof surface plasmon, on real metals. In their derivation, the long-wavelength approximation is assumed, i.e., the characteristic length of the structure are much smaller than the wavelength, and therefore the structured metal can be described as a homogeneous medium with effective dielectric constant and permeability. If a structure with characteristic length comparable to incoming wavelength is considered, the spoof surface plasmon still exists. In this case, the diffracted modes have also to be considered, and the main effect of the diffraction is to couple the confined spoof surface plasmon to free space. Therefore, an anomaly optical transmission can also occur when the incident light resonantly excites this surface mode. In the following part of the thesis, our theoretical ground will base on this result.

Chapter 2 Method of Measurement

We used Fourier Transform Infrared Spectroscopy (FTIR) as our measurement method to analyze the transmission spectra of the devices under study in THz region. In this chapter, we will briefly introduce the fundamentals of FTIR method and the details of this measurement instrument. **Fig. 2.1** is the basic schematics of a Michelson interferometer. A mercury lamp is used as the far-infrared light source. When light impinges on the beam splitter (50% transmitted and 50% reflected), the differences of light path can be adjusted by moving the mirrors, M1 and M2. In our instrument, M1 is held fixed while M2 is varied. As **Fig. 2.1** shows, the reflected part of the light that goes to the fixed M1 in a distance L is reflected there and impinges on the beam splitter again after a total path of $2L$. The same action happens to the transmitted part of the beam. Nevertheless, since the reflecting mirror M2 is not held fixed but can be moved very precisely back and forth around L by a distance x , the total path length of this light is consequently $2(L+x)$. Then, when the two halves of the light recombine again on the beam splitter, they possess a path length difference of $2x$ and thus show a interference pattern. The light leaving the interferometer is then passed through the sample under test and is finally focused on the detector. In fact, the quantity measured by the detector is the intensity $I(x)$ which is a function of moving mirror displacement x , the so-called interferogram. Here we use the zero crossings of the interferogram of He-Ne laser to sample that of the sample under measurement.

One of the advantages of FTIR is its measurement accuracy. The accuracy of the sampling spacing between two zero crossings is only determined by the precision of the laser wavelength itself. And the common FTIR spectrometers have a built-in

wavenumber calibration of high precision of about 0.01 cm^{-1} . Besides its high accuracy, FTIR has others prior features to conventional IR grating spectrometers: the signal intensity. Because the circular apertures used in FTIR spectrometers have a larger area than the linear slit used in grating spectrometers, the throughput of light can be enhanced considerably. It is especially useful to the far-infrared measurement since the power density of general far-infrared light source is very weak. After data acquisition, we cannot directly read the spectrum information. The digitized, discrete and equidistant interferogram $I(x)$ must be converted to a spectrum $S(k\nu)$ by discrete Fourier transformation (DFT):

$$S(k \cdot \Delta\nu) = \sum_{n=0}^{N-1} I(n \cdot \Delta x) \exp(i2\pi nk / N), \quad (2.1)$$

where $S(k \cdot \Delta\nu)$ is the magnitude of the spectrum, $I(n \cdot \Delta x)$ is the magnitude of

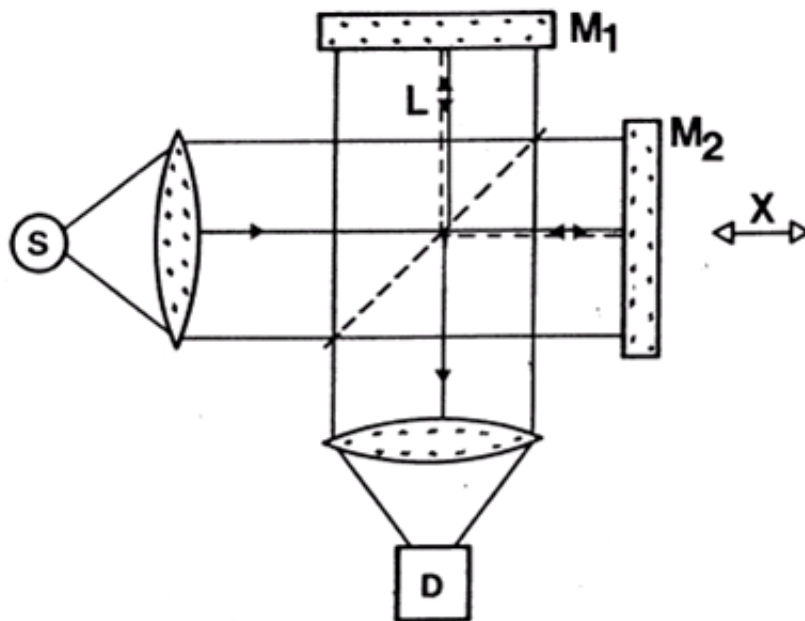


Fig. 2.1 Schematics of a Michelson interferometer. S: light source. D: detector. M1: fixed mirror. M2: movable mirror. X: mirror displacement.

interferogram, Δx is the sampling distance, and $\Delta \nu$ is the interval of the frequency of the spectrum. The relation between $\Delta \nu$ and Δx is as the following,

$$\Delta \nu = \frac{1}{N \cdot \Delta x}, \quad (2.2)$$

where N is the number of sampling points.

The interferogram $I(n \cdot \Delta x)$ can be reconstructed by inverse discrete Fourier transformation (IDFT):

$$I(n \cdot \Delta x) = \frac{1}{N} \sum_{k=0}^{N-1} S(k \cdot \Delta \nu) \exp(-\frac{i2\pi nk}{N}). \quad (2.3)$$

The above is the mathematical fundamental of DFT. **Fig. 2.2** shows some examples of Fourier Transform. The final transmittance spectrum can be obtained by three steps: a) an interferogram measured without sample in the optical path is Fourier transformed and generates the single channel reference spectrum $R(\nu)$ (referred to **Fig. 2.3(a)**); b) an interferogram with a sample in the optical path is measured and Fourier transformed and generate the single channel sample spectrum $S(\nu)$ (referred to **Fig. 2.3(b)**); c) the final transmittance spectrum $T(\nu)$ is defined as $T(\nu) = \frac{S(\nu)}{R(\nu)}$ (referred to **Fig. 2.3(c)**). To further eliminate the H_2O and CO_2 absorptions in THz region of the optical path, we vacuum the chamber for every measurement. Some typical spectrums are shown in **Fig. 2.3**.

The type of FTIR instrument in our lab is “Bruker IFs66vs”, and the measurement wavenumber range of liquid-He-cooled bolometer is from 50 cm^{-1} to 700 cm^{-1} which is equal to $14 \mu\text{m}$ to $200 \mu\text{m}$ in wavelength.

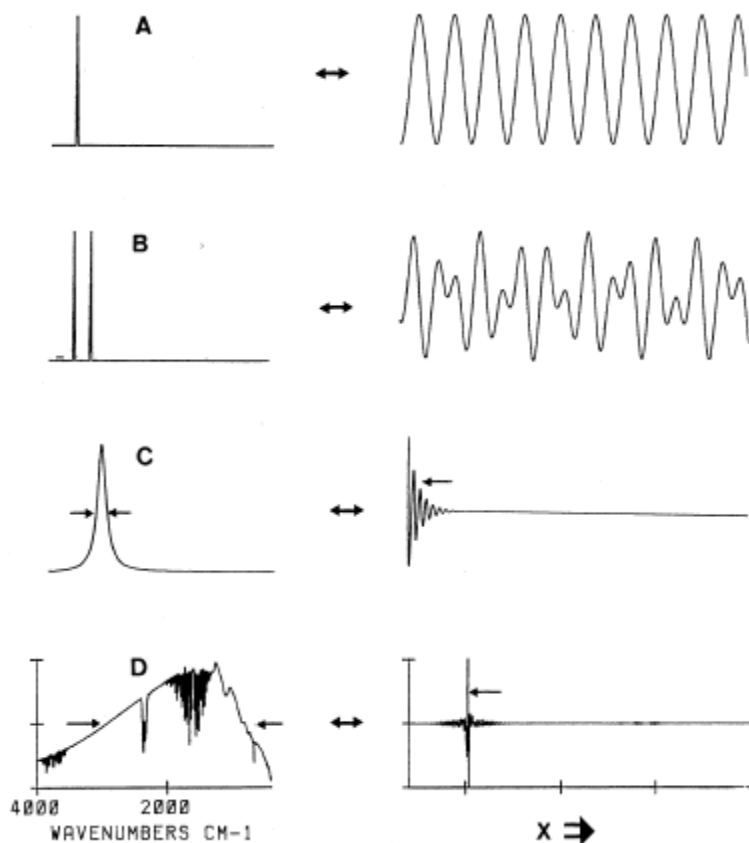


Fig. 2.2 Examples of spectra (left side) and their corresponding interferograms (right side).

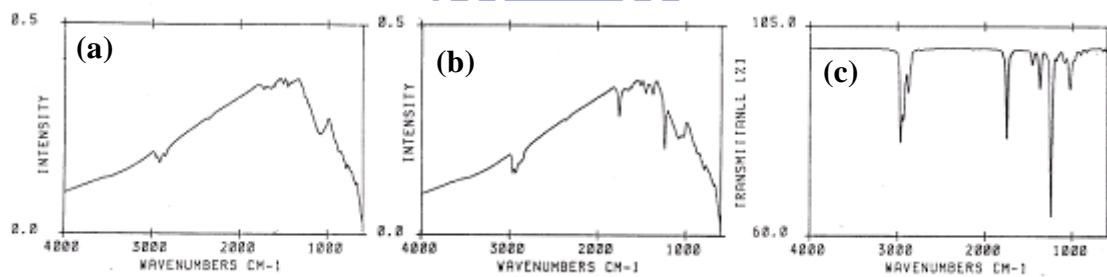


Fig. 2.3 Three kinds of transmission spectra: (a) reference spectrum, (b) spectrum of absorbing sample, (c) transmittance spectrum obtained by dividing (b) by (a).

Chapter 3 Sample Design and Fabrication

Fig. 3.1 depicts the general profile of the samples fabricated by standard microlithography process. We defined the pattern by photolithography after coating the substrate surface with photoresist and then deposited 20nm-thick titanium for adhesive layer on intrinsic $1\text{cm}\times 1\text{cm}$ GaAs ($\epsilon_{\text{GaAs}} = 13.7$) substrate and 200nm-thick gold successively. Finally, a 2D hole array was perforated on the metal by lift-off process. The pattern on the metal was indeed a 2D Bravais lattice. It is known that there are five types of 2D Bravais lattices. Here we chose four types of lattices, which are square, rectangular, oblique, and triangular, to investigate the EOT phenomenon. To investigate the influence of hole shape on the transmission spectra, we varied the hole shape of the array with fixed periodicity. Especially we focused on square array with different hole shapes. As **Fig. 3.2(a)** shows, for square arrays, we varied the hole widths from $18\ \mu\text{m}$ to $3\ \mu\text{m}$ and with the hole lengths unchanged. In **Fig. 3.2(b)** we did the same work but started the shrinking from $14\ \mu\text{m}$. It is shown that both spectra in **Fig. 3.2** have non-monotonous redshifts as the aspect ratios of holes are very large. On the other hand, we made the same pattern as **Fig. 3.2(b)** but with different metal, titanium, of 200nm thickness to see the influence of finite conductivity, as shown in **Fig. 3.3**. The finite conductivity effect can result in larger loss and enlarge the cutoff wavelength of the holes [26]. In **Fig. 3.4**, we kept the aspect ratio of the holes unchanged but shrank hole area gradually, and we found that the peak positions of the spectrum blueshift with decreasing full width at half maximum (FWHM). Moreover, we also studied the effect of symmetry difference between hole and lattice. It is known that any Bravais lattice has its unique primitive unit cell which is called Wigner-Seitz cell. A Wigner-Seitz cell has the full symmetry

of the Bravais lattice, i.e., the Wigner-Seitz cell is as symmetrical as the Bravais lattice. Therefore, for each lattice, we defined the hole by Wigner-Seitz cell of the lattice. We found that if we kept the same symmetry but shrank the hole area, the peak position would be unchanged. The results are shown in **Fig. 3.5(a)-(d)**. There is one thing that has to be mentioned: in **Fig. 3.5(b)**, **Fig. 3.5(c)** and **Fig. 3.5(d)** the substrate material is changed to intrinsic silicon and the metal we use is 200nm-thick aluminum for economic consideration. The detailed discussion about these measurement results can be postponed until Chapter 5.





Fig. 3.1(a) Top-view of the sample under measurement. The gray region represents the substrate while the yellow region is the metal. (colors)



Fig. 3.1(b) Side-view of the sample under measurement. (colors)

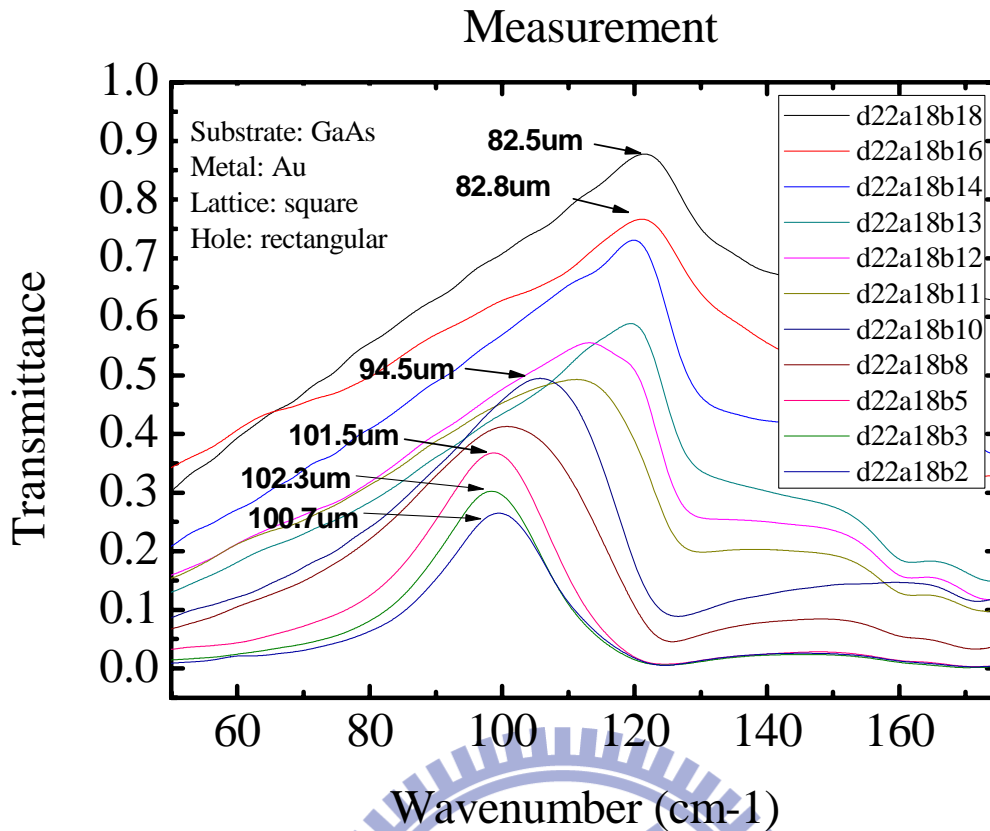


Fig. 3.2(a) Evolution of transmittance with various aspect ratios. d: lattice constant. a: the length of rectangular hole. b: the width of rectangular hole. (colors)

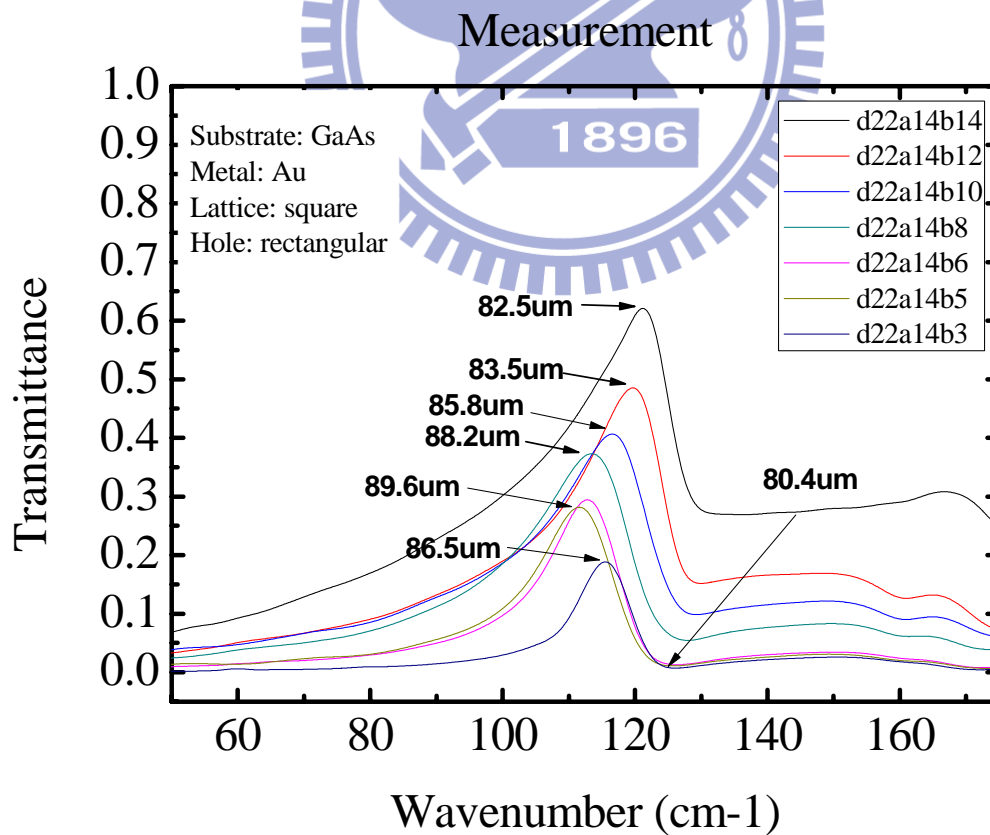


Fig. 3.2(b) Evolution of transmittance with various aspect ratios. d: lattice constant. a: the length of rectangular hole. b: the width of rectangular hole. (colors)

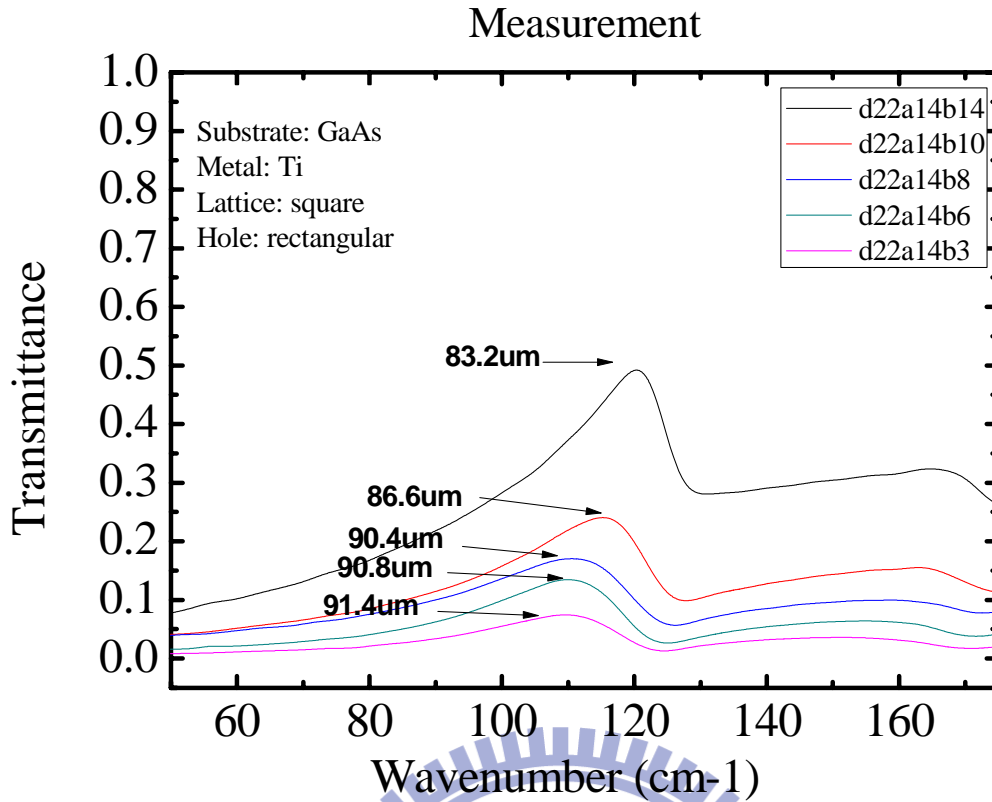


Fig. 3.3 Evolution of transmittance with low-conductive metal. d: lattice constant. a: the length of rectangular hole. b: the width of rectangular hole. (colors)

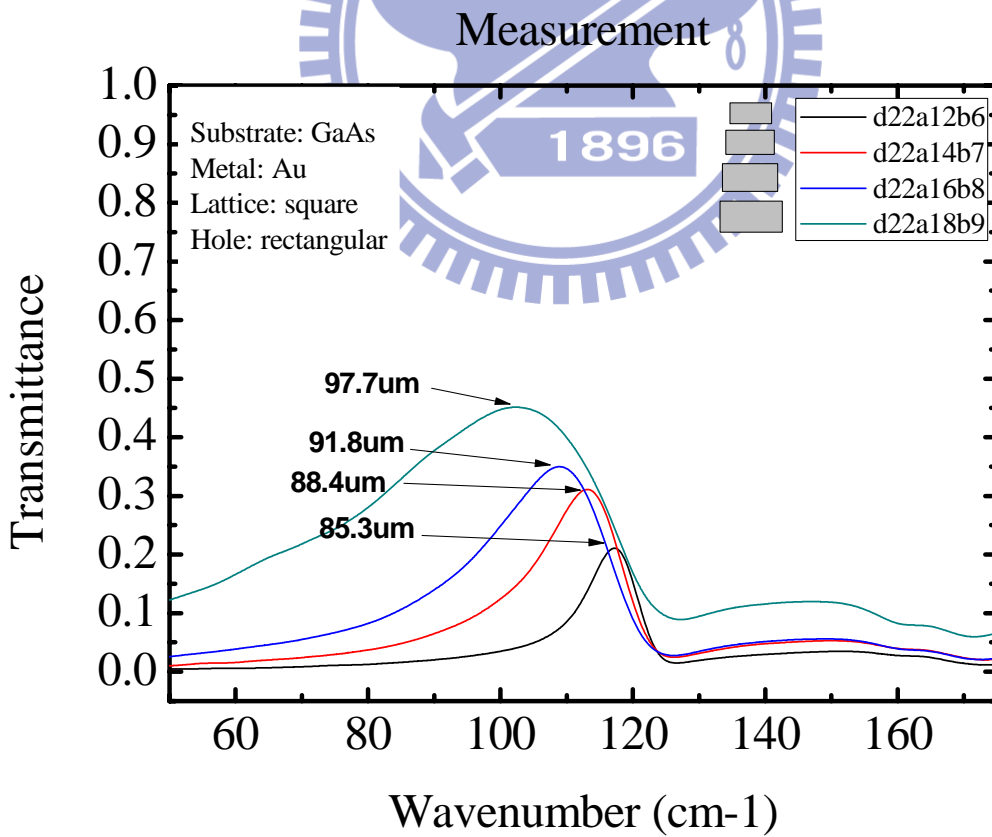


Fig. 3.4 Transmission spectra with fixed aspect ratio of the holes. d: lattice constant. a: the length of rectangular hole. b: the width of rectangular hole. (colors)

Measurement: Square Lattice

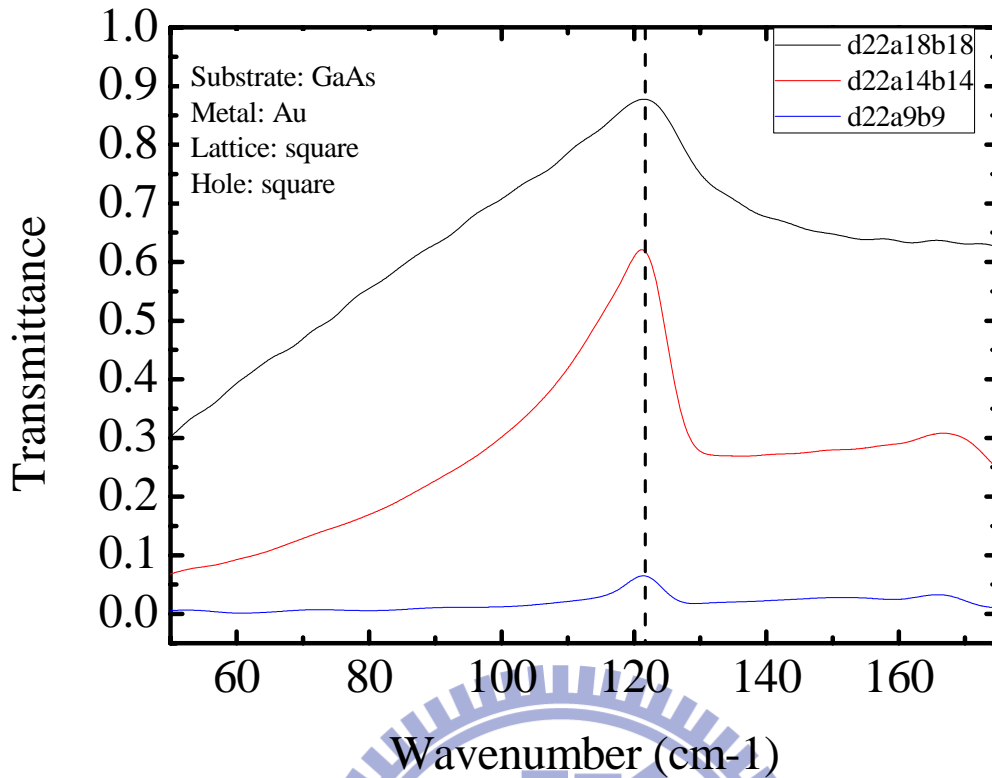


Fig. 3.5 (a) Evolution of transmittance with same symmetry between hole and lattice. (colors)

Measurement: Rectangular Lattice

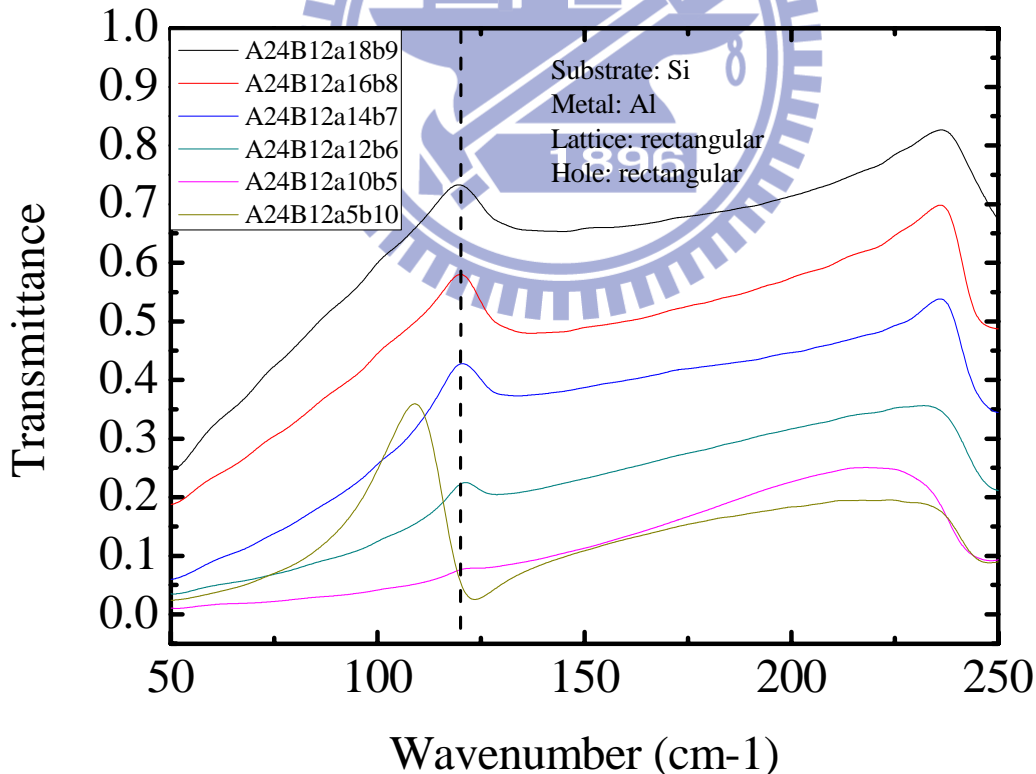


Fig. 3.5 (b) Evolution of transmittance with same symmetry between hole and lattice. “A” and “B” represent the rectangular lattice constants in x- and y-direction respectively. “a” and “b” represent the hole sides with the same direction as “A” and “B” respectively. (colors)

Measurement: Oblique Lattice

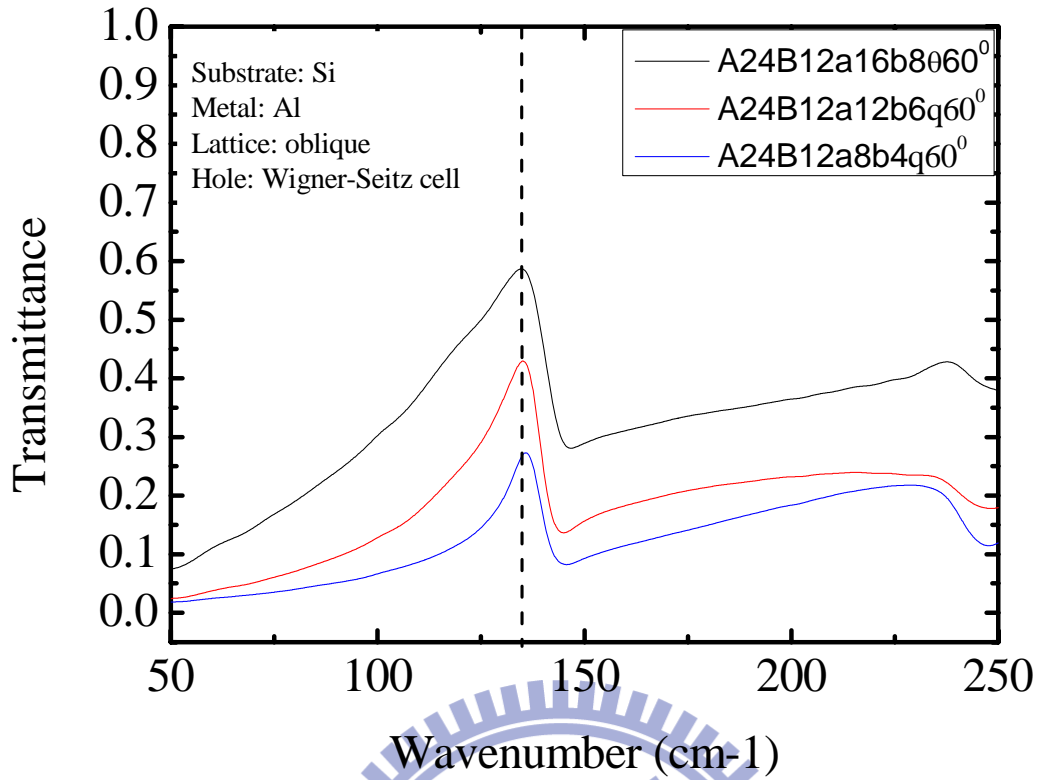


Fig. 3.5 (c) Evolution of transmittance with same symmetry between hole and lattice. (colors)

Measurement: Triangular Lattice

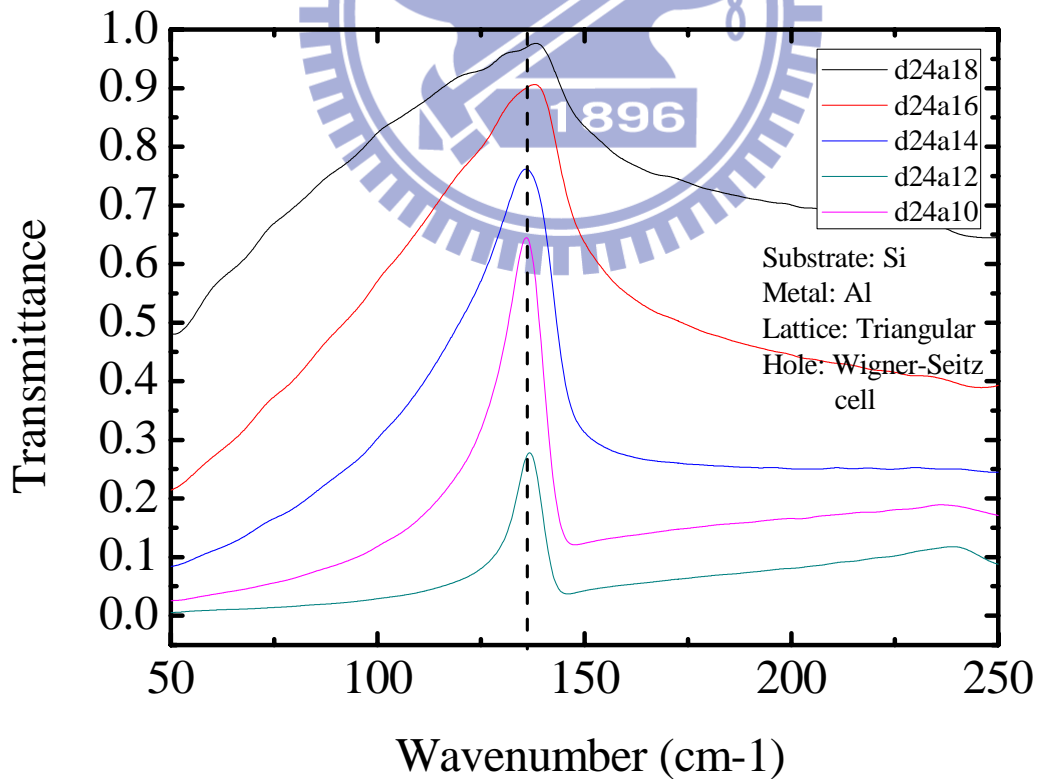


Fig. 3.5 (d) Evolution of transmittance with same symmetry between hole and lattice.. “d” represents the lattice constant. “a” represents the side length of Wigner-Seitz cell of triangular lattice. (colors)

Chapter 4 Theoretical Formalism

In order to analyze the experimental data and understand the physics involved in the 2D structure, we have to do the calculation based on modal expansion. The unit system we adapt here is SI units.

First of all, we divide the whole system into three regions which are I, II, and III respectively as shown in **Fig. 4.1(b)**. Region I is the region of reflection where the EM fields can be expanded by the eigenmodes of Helmholtz's equations in free space and the incident light is given in this region. Region II is the structure region where the EM fields inside the hole can be expanded by rectangular waveguide modes of perfect electrical conductor (PEC). Region III is the substrate region which can be seen as another kind of free space except the light velocity there has to be divided by refraction index of the substrate material. The 2D structure under study is an infinite array of holes drilled periodically in a metal film of thickness h . **Fig. 4.1(a)** depicts the definition of the primitive unit cell. The primitive unit cell is defined as a rectangular with length and width being A , B respectively, while the length and width of the rectangular hole inside the unit cell is denoted by a , b respectively.

We start from the Maxwell's equations for complex time-harmonic fields in source free case:

$$\nabla \times \mathbf{H}(\mathbf{r}) - i\omega\mu_0\mathbf{E}(\mathbf{r}) = 0 \quad (4.1)$$

$$\nabla \times \mathbf{E}(\mathbf{r}) + i\omega\varepsilon_0\varepsilon(\mathbf{r})\mathbf{H}(\mathbf{r}) = 0 \quad (4.2)$$

$$\nabla \cdot \mathbf{H}(\mathbf{r}) = 0 \quad (4.3)$$

$$\nabla \cdot \varepsilon_0 \varepsilon(\mathbf{r}) \mathbf{E}(\mathbf{r}) = 0, \quad (4.4)$$

where the related coefficients are the same as the standard notations in any electromagnetic textbook. In the following derivation, the only approximation we make is that the metal is considered to be perfect electrical conductor (PEC). This is a good approximation because our system is operated in THz region, where the skin depth of the metal with good conductivity is about only several tens of nanometer. Combine (4.1) and (4.2), we obtain

$$\nabla \times \left(\frac{1}{\varepsilon_0 \varepsilon(\mathbf{r})} \nabla \times \mathbf{H} \right) = \left(\frac{\omega}{c} \right)^2 \mathbf{H} \quad (4.5)$$

$$\nabla \times (\nabla \times \mathbf{E}) = \varepsilon_0 \varepsilon(\mathbf{r}) \left(\frac{\omega}{c} \right)^2 \mathbf{E}. \quad (4.6)$$

After further manipulation we can obtain two Helmholtz's equations,

$$\nabla^2 \mathbf{E}(\mathbf{r}) + \varepsilon_0 \varepsilon(\mathbf{r}) \left(\frac{\omega}{c} \right)^2 \mathbf{E}(\mathbf{r}) = 0 \quad (4.7)$$

and

$$\nabla^2 \mathbf{H}(\mathbf{r}) + \mu_0 \left(\frac{\omega}{c} \right)^2 \mathbf{H}(\mathbf{r}) = 0. \quad (4.8)$$

Both electric and magnetic fields satisfy the above two Helmholtz's equations in each region. At any boundary the EM fields in between the regions satisfy the following boundary conditions,

$$\mathbf{n} \cdot (\mu_1 \mathbf{H}_1 - \mu_2 \mathbf{H}_2) = 0 \quad (4.9)$$

$$\mathbf{n} \times (\mathbf{H}_1 - \mathbf{H}_2) = \mathbf{J}_s \quad (4.10)$$

$$\mathbf{n} \cdot (\varepsilon_1 \mathbf{E}_1 - \varepsilon_2 \mathbf{E}_2) = \rho_s \quad (4.11)$$

$$\mathbf{n} \times (\mathbf{E}_1 - \mathbf{E}_2) = 0, \quad (4.12)$$

where the numbers of subscripts mean different regions, \mathbf{n} is the unitary vector normal to the surface, and \mathbf{J}_s and ρ_s are surface current and surface charge respectively. In the following, we will first attack this problem at each region individually and then match the boundary conditions at the interface of each region. All EM fields at each region are governed by (4.7) and (4.8). To simplify the derivation, we learned from Garcia's paper in 2008 [16] to use Dirac's notation for representation of each field, or eigenfunction. For example, the electric field can be written as $\mathbf{E}(\mathbf{r}) = \langle \mathbf{r}_// | \mathbf{E} \rangle E(z)$. The reason why we deliberately separate the z-dependent function from Dirac's notation will be apparent in our derivation soon. To further simplify the derivation, according to Garcia, for the same mode E-field and H-field have the following relation

$$\langle -\mathbf{z} \times \mathbf{H}_{\text{mode}} \rangle = \pm Y_{\text{mode}} \langle \mathbf{E}_{\text{mode}} \rangle, \quad (4.13)$$

where Y_{mode} is the modal admittance. The choice of + or - depends on the propagation direction +z or -z respectively. Consequently we can consider only the eigenmodes of electric field.

Basically, we can categorize the system into two types, the free space type and the inside hole type. In free space, the eigenmodes of (4.7) are plane waves obeying Bragg diffraction law, i.e., $\mathbf{k} = \mathbf{k}_0 + \mathbf{G}$, where \mathbf{k}_0 and \mathbf{k} are incident and reflected wavevectors respectively, and $\mathbf{G} = 2\pi(\frac{m}{A}\mathbf{x} + \frac{n}{B}\mathbf{y})$. In the previous expression (m, n) denoting the diffraction order is a pair of arbitrary integers. Moreover, the plane wave eigenmodes can be further decomposed to two orthogonal functions based on the directions of polarization, p and s. The definitions of p- and s-polarizations are shown in **Fig. 4.1(c)**. Thus the eigenmodes in free space region is denoted by $|mnp\rangle$ and $|mns\rangle$. Inside the hole, the eigenmodes of (4.7) are rectangular waveguide modes

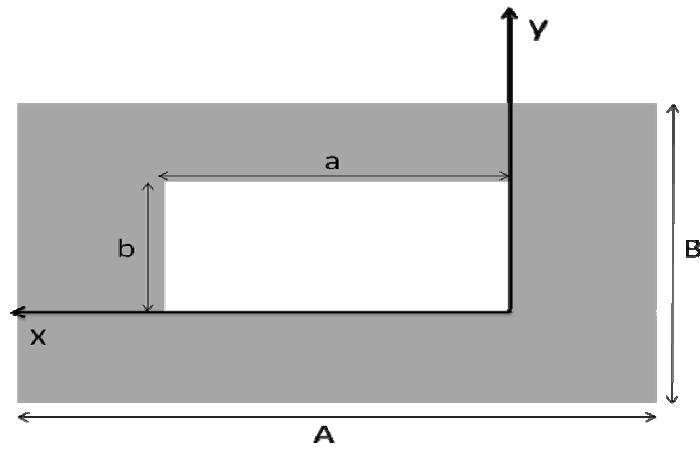


Fig. 4.1(a) Top view of unit cell of the rectangular lattice.

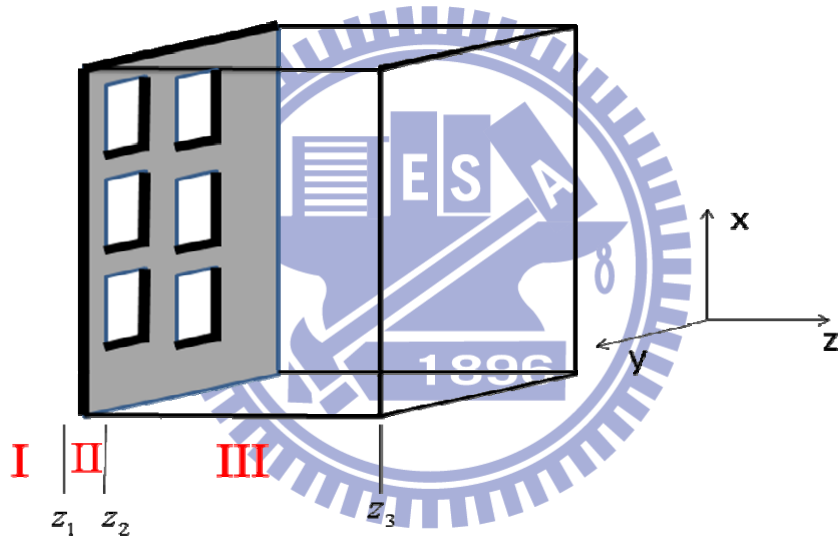


Fig. 4.1(b) Schematics of the system under study.

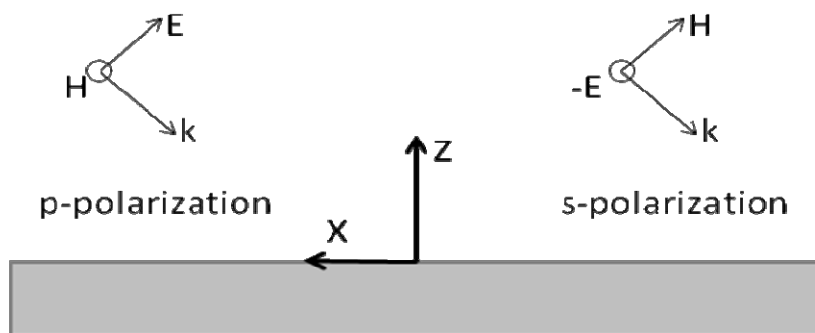


Fig. 4.1(c) Schematics of the system with incident light.

which can be denoted by $|\text{TE},pq\rangle$ and $|\text{TM},pq\rangle$, where (p,q) represents a certain order of waveguide mode.

After choosing the expansion basis with consideration of Bloch's theorem, we can write down the EM fields in different regions:

- Region I, ($z < 0$)

Given a normal incident wave, the EM fields can be expressed as follows,

$$|\mathbf{E}^I(z)\rangle = \left\{ a_{\text{inc},p}^{(1)} |00p\rangle + a_{\text{inc},s}^{(1)} |00s\rangle \right\} e^{ik_{z,00}^{(1)}(z-z_1)} + \sum_{mn} \left[b_{mnp}^{(1)} |mnp\rangle e^{-ik_{z,mn}^{(1)}(z-z_1)} + b_{mns}^{(1)} |mns\rangle e^{-ik_{z,mn}^{(1)}(z-z_1)} \right] \quad (4.14)$$

$$|-\mathbf{z} \times \mathbf{H}^I(z)\rangle = \left\{ a_{\text{inc},p}^{(1)} Y_{00p}^{(1)} |00p\rangle + a_{\text{inc},s}^{(1)} Y_{00s}^{(1)} |00s\rangle \right\} e^{ik_{z,00}^{(1)}(z-z_1)} - \sum_{mn} \left[b_{mnp}^{(1)} |mnp\rangle Y_{mnp}^{(1)} e^{-ik_{z,mn}^{(1)}(z-z_1)} + b_{mns}^{(1)} |mns\rangle Y_{mns}^{(1)} e^{-ik_{z,mn}^{(1)}(z-z_1)} \right], \quad (4.15)$$

where

$$k_{z,mn}^{(1)} = \sqrt{\left(\frac{\omega}{c}\right)^2 - \left(\frac{2\pi m}{A}\right)^2 - \left(\frac{2\pi n}{B}\right)^2} \quad (4.16)$$

$$Y_{mnp}^{(1)} = \frac{\omega \varepsilon_0}{k_{z,mn}^{(1)}} \quad (4.17)$$

$$Y_{mns}^{(1)} = \frac{k_{z,mn}^{(1)}}{\omega \mu_0} \quad (4.18)$$

and $b_{mnp}^{(1)}$, $b_{mns}^{(1)}$ are coefficients to be calculated.

- Region II, ($z_1 < z < z_2$)

$$|\mathbf{E}^{II}(z)\rangle = \sum_{\mathbf{R}} e^{ik_0 \cdot \mathbf{R}} \left[\sum_{pq} |\text{TM},pq, \mathbf{R}\rangle \left(a_{\text{TM},pq}^{(2)} e^{ik_{z,pq}^{(2)}(z-z_1)} + b_{\text{TM},pq}^{(2)} e^{-ik_{z,pq}^{(2)}(z-z_2)} \right) + \sum_{pq} |\text{TE},pq, \mathbf{R}\rangle \left(a_{\text{TE},pq}^{(2)} e^{ik_{z,pq}^{(2)}(z-z_1)} + b_{\text{TE},pq}^{(2)} e^{-ik_{z,pq}^{(2)}(z-z_2)} \right) \right] \quad (4.19)$$

$$|-\mathbf{z} \times \mathbf{H}^{\text{II}}(z)\rangle = \sum_{\mathbf{R}} e^{i\mathbf{k}_0 \cdot \mathbf{R}} \left[\sum_{pq} Y_{\text{TM},pq}^{(2)} |\text{TM},pq, \mathbf{R}\rangle \left(a_{\text{TM},pq}^{(2)} e^{ik_{z,pq}^{(2)}(z-z_1)} - b_{\text{TM},pq}^{(2)} e^{-ik_{z,pq}^{(2)}(z-z_2)} \right) + \sum_{pq} Y_{\text{TE},pq}^{(2)} |\text{TE},pq, \mathbf{R}\rangle \left(a_{\text{TE},pq}^{(2)} e^{ik_{z,pq}^{(2)}(z-z_1)} - b_{\text{TE},pq}^{(2)} e^{-ik_{z,pq}^{(2)}(z-z_2)} \right) \right] \quad (4.20)$$

, where

$$k_{z,pq}^{(2)} = \sqrt{\left(\frac{\omega}{c}\right)^2 - \left(\frac{\pi p}{a}\right)^2 - \left(\frac{\pi q}{b}\right)^2} \quad (4.21)$$

$$Y_{\text{TM},pq}^{(2)} = \frac{\omega \mathcal{E}_0}{k_{z,pq}^{(2)}} \quad (4.22)$$

$$Y_{\text{TE},pq}^{(2)} = \frac{k_{z,pq}^{(2)}}{\omega \mu_0} \quad (4.23)$$

\mathbf{R} is the position vector on the x-y plane and $a_{\text{TM},pq}^{(2)}$, $a_{\text{TE},pq}^{(2)}$, $b_{\text{TM},pq}^{(2)}$, $b_{\text{TE},pq}^{(2)}$ are coefficients to be calculated.

- Region III, ($z > z_2$)

$$|\mathbf{E}^{\text{III}}(z)\rangle = \sum_{mn} \left[a_{mnp}^{(3)} |mnp\rangle e^{ik_{z,mn}^{(3)}(z-z_2)} + a_{mns}^{(3)} |mns\rangle e^{ik_{z,mn}^{(3)}(z-z_2)} \right] \quad (4.24)$$

$$|-\mathbf{z} \times \mathbf{H}^{\text{III}}(z)\rangle = \sum_{mn} \left[a_{mnp}^{(3)} |mnp\rangle Y_{mnp}^{(3)} e^{ik_{z,mn}^{(3)}(z-z_2)} + a_{mns}^{(3)} |mns\rangle Y_{mns}^{(3)} e^{ik_{z,mn}^{(3)}(z-z_2)} \right], \quad (4.25)$$

where

$$k_{z,mn}^{(3)} = \sqrt{\left(\frac{\omega}{c}\right)^2 \mathcal{E}_{\text{GaAs}} - \left(\frac{2\pi m}{A}\right)^2 - \left(\frac{2\pi n}{B}\right)^2} \quad (4.26)$$

$$Y_{mnp}^{(3)} = \frac{\omega \mathcal{E}_0 \mathcal{E}_{\text{GaAs}}}{k_{z,mn}^{(3)}} \quad (4.27)$$

$$Y_{mns}^{(3)} = \frac{k_{z,mn}^{(3)}}{\omega \mu_0} \quad (4.28)$$

and $a_{mnp}^{(3)}$, $a_{mns}^{(3)}$ are coefficients to be calculated.

Now we write down the real space expression for each eigenmode explicitly:

$$\langle \mathbf{r}_{//} | mnp \rangle = \frac{1}{\sqrt{AB \left[\left(\frac{2\pi m}{A} \right)^2 + \left(\frac{2\pi n}{B} \right)^2 \right]}} \begin{bmatrix} \frac{2\pi m}{A} \\ \frac{2\pi n}{B} \end{bmatrix} e^{i \left(\frac{2\pi m}{A} x + \frac{2\pi n}{B} y \right)} \quad (4.29)$$

, if m, n are nonzero.

$$\langle \mathbf{r}_{//} | mns \rangle = \frac{1}{\sqrt{AB \left[\left(\frac{2\pi m}{A} \right)^2 + \left(\frac{2\pi n}{B} \right)^2 \right]}} \begin{bmatrix} \frac{-2\pi n}{B} \\ \frac{2\pi m}{A} \end{bmatrix} e^{i \left(\frac{2\pi m}{A} x + \frac{2\pi n}{B} y \right)} \quad (4.30)$$

, if m, n are nonzero.

$$\langle \mathbf{r}_{//} | 00p \rangle \equiv \frac{1}{\sqrt{AB}} \begin{bmatrix} 1 \\ 0 \end{bmatrix} \quad (4.31)$$

$$\langle \mathbf{r}_{//} | 00s \rangle \equiv \frac{1}{\sqrt{AB}} \begin{bmatrix} 0 \\ 1 \end{bmatrix} \quad (4.32)$$

$$\langle \mathbf{r}_{//} | \text{TM}, pq, \mathbf{R} \rangle = \frac{1}{\sqrt{ab \left[\left(\frac{\pi p}{a} \right)^2 + \left(\frac{\pi q}{b} \right)^2 \right]}} \begin{bmatrix} \frac{2\pi p}{a} \cos \left(\frac{p\pi}{a} (x - R_x) \right) \sin \left(\frac{q\pi}{b} (y - R_y) \right) \\ \frac{2\pi q}{b} \sin \left(\frac{p\pi}{a} (x - R_x) \right) \cos \left(\frac{q\pi}{b} (y - R_y) \right) \end{bmatrix}, \quad (4.33)$$

if p, q are nonzero.

$$\langle \mathbf{r}_{//} | \text{TE}, pq, \mathbf{R} \rangle = \frac{1}{\sqrt{ab \left[\left(\frac{\pi p}{a} \right)^2 + \left(\frac{\pi q}{b} \right)^2 \right]}} \begin{bmatrix} \frac{-2\pi q}{b} \cos \left(\frac{p\pi}{a} (x - R_x) \right) \sin \left(\frac{q\pi}{b} (y - R_y) \right) \\ \frac{2\pi p}{a} \sin \left(\frac{p\pi}{a} (x - R_x) \right) \cos \left(\frac{q\pi}{b} (y - R_y) \right) \end{bmatrix}, \quad (4.34)$$

if p, q are nonzero.

There is one important thing that has to be mentioned. For TE waveguide modes,

$\langle \mathbf{r}_{//} | \text{TE}, pq \rangle$, if $p = 0$ or $q = 0$, the normalization must be amended by multiplication

of the right-hand side of (4.34) by $\frac{1}{\sqrt{2}}$. Now it is time to match the boundary

conditions. Using (4.10) and (4.12) we know that the electric fields parallel to the

surface have to be continuous everywhere on the surface and magnetic fields parallel to the surface have to be continuous on the holes area. Therefore, as Garcia did, we project the matching equations onto plane wave eigenmodes for electric fields and rectangular waveguide eigenmodes for magnetic fields. Besides, we can match the boundary only on one Wigner-Seitz unit cell, i.e., $\mathbf{R} = 0$, because our structure has perfect periodicity and thus satisfies Bloch's theorem. Therefore we can abbreviate $|\text{TM}, pq, \mathbf{R} = 0\rangle$ and $|\text{TE}, pq, \mathbf{R} = 0\rangle$ to $|\text{TM}, pq\rangle$ and $|\text{TE}, pq\rangle$ respectively. The boundary conditions are matched at two interfaces:

At $z = z_1$ ($z_1 - z_2 = -h$):

For E-field,

$$|\mathbf{E}^I(z = z_1)\rangle = |\mathbf{E}^{II}(z = z_1)\rangle. \quad (4.35)$$

Then multiply (4.35) by $\langle mnp|$ and $\langle mns|$ separately and do integration over an area of unit cell to obtain

$$\left\{ a_{\text{inc},p}^{(1)} \delta_{m0} \delta_{n0} \delta_{\sigma p} + a_{\text{inc},s}^{(1)} \delta_{m0} \delta_{n0} \delta_{\sigma s} \right\} + b_{mn\sigma}^{(1)} = \sum_{pq} \langle mn\sigma | \text{TM}, pq \rangle \left(a_{\text{TM},pq}^{(2)} + b_{\text{TM},pq}^{(2)} e^{ik_z^{(2)} pq h} \right) + \sum_{pq} \langle mn\sigma | \text{TE}, pq \rangle \left(a_{\text{TE},pq}^{(2)} + b_{\text{TE},pq}^{(2)} e^{ik_z^{(2)} pq h} \right), \quad (4.36)$$

where

$$\sigma = p, s \quad (4.37)$$

$$\delta_{mn} = \begin{cases} 1, & \text{if } m = n \\ 0, & \text{if } m \neq n \end{cases}. \quad (4.38)$$

For H-field,

$$|-\mathbf{z} \times \mathbf{H}^I(z = z_1)\rangle = |-\mathbf{z} \times \mathbf{H}^{II}(z = z_1)\rangle \quad (4.39)$$

Then multiply (4.39) by $\langle \text{TM}, pq|$ and $\langle \text{TE}, pq|$ separately and do integration over

an area of a hole to obtain

$$\begin{aligned} & \left\{ a_{\text{inc},p}^{(1)} Y_{00p}^{(1)} \langle \alpha | 00p \rangle + a_{\text{inc},s}^{(1)} Y_{00s}^{(1)} \langle \alpha | 00s \rangle \right\} - \\ & \sum_{mn} \left[b_{mnp}^{(1)} Y_{mnp}^{(1)} \langle \alpha | mnp \rangle + b_{mns}^{(1)} Y_{mns}^{(1)} \langle \alpha | mns \rangle \right] = Y_{\alpha,pq}^{(2)} \left(a_{\alpha,pq}^{(2)} - b_{\alpha,pq}^{(2)} e^{ik_{z,pq}^{(2)}h} \right), \end{aligned} \quad (4.40)$$

where

$$\alpha = \text{TM, TE}. \quad (4.41)$$

At $z = z_2$ ($z_2 - z_1 = h$):

For E-field,

$$\left| \mathbf{E}^{\text{III}}(z = z_2) \right\rangle = \left| \mathbf{E}^{\text{II}}(z = z_2) \right\rangle \quad (4.42)$$

Then multiply (4.42) by $\langle mnp |$ and $\langle mns |$ separately and integrate over the area of unit cell to obtain

$$\begin{aligned} a_{mn\sigma}^{(1)} = & \sum_{pq} \langle mn\sigma | \text{TM}, pq \rangle \left(a_{\text{TM},pq}^{(2)} e^{ik_{z,pq}^{(2)}h} + b_{\text{TM},pq}^{(2)} \right) + \\ & \sum_{pq} \langle mn\sigma | \text{TE}, pq \rangle \left(a_{\text{TE},pq}^{(2)} e^{ik_{z,pq}^{(2)}h} + b_{\text{TE},pq}^{(2)} \right), \end{aligned} \quad (4.43)$$

where

$$\sigma = p, s. \quad (4.44)$$

For H-field,

$$\left| -\mathbf{z} \times \mathbf{H}^{\text{III}}(z = z_2) \right\rangle = \left| -\mathbf{z} \times \mathbf{H}^{\text{II}}(z = z_2) \right\rangle \quad (3.45)$$

$$\sum_{mn} \left[a_{mnp}^{(3)} Y_{mnp}^{(3)} \langle \alpha | mnp \rangle + a_{mns}^{(3)} Y_{mns}^{(3)} \langle \alpha | mns \rangle \right] = Y_{\alpha,pq}^{(2)} \left(a_{\alpha,pq}^{(2)} e^{ik_{z,pq}^{(2)}h} - b_{\alpha,pq}^{(2)} \right) \quad (4.46)$$

where

$$\alpha = \text{TM, TE}. \quad (4.47)$$

With the four simultaneous equations (4.36), (4.40), (4.43), and (4.46), we can determine the coefficients $b_{mn\sigma}^{(1)}$, $a_{\alpha,pq}^{(2)}$, $b_{\alpha,pq}^{(2)}$, and $b_{mn\sigma}^{(3)}$.

Now we express (4.36), (4.40), (4.43), and (4.46) in matrix forms:

$$[\mathbf{M}] = \begin{bmatrix} \langle mnp | \text{TM}, pq \rangle & \cdots & \langle mnp | \text{TE}, pq \rangle & \cdots \\ \vdots & \ddots & \vdots & \ddots \\ \langle mns | \text{TM}, pq \rangle & \cdots & \langle mns | \text{TE}, pq \rangle & \cdots \\ \vdots & \ddots & \vdots & \ddots \end{bmatrix} \quad (4.48)$$

$$[\mathbf{E}] = \begin{bmatrix} e^{ik_z^{(2)}h} & 0 & \cdots & 0 \\ 0 & \ddots & 0 & \vdots \\ \vdots & 0 & e^{ik_z^{(2)}h} & 0 \\ 0 & \cdots & 0 & \ddots \end{bmatrix} \quad (4.49)$$

$$[\mathbf{Y}_1] = \begin{bmatrix} Y_{mnp}^{(1)} & 0 & \cdots & 0 \\ 0 & \ddots & 0 & \vdots \\ \vdots & 0 & Y_{mns}^{(1)} & 0 \\ 0 & \cdots & 0 & \ddots \end{bmatrix} \quad (4.50)$$

$$[\mathbf{Y}_2] = \begin{bmatrix} Y_{\text{TM},pq}^{(2)} & 0 & \cdots & 0 \\ 0 & \ddots & 0 & \vdots \\ \vdots & 0 & Y_{\text{TE},pq}^{(2)} & 0 \\ 0 & \cdots & 0 & \ddots \end{bmatrix} \quad (4.51)$$

$$[\mathbf{Y}_3] = \begin{bmatrix} Y_{mnp}^{(3)} & 0 & \cdots & 0 \\ 0 & \ddots & 0 & \vdots \\ \vdots & 0 & Y_{mns}^{(3)} & 0 \\ 0 & \cdots & 0 & \ddots \end{bmatrix} \quad (4.52)$$

$$[\mathbf{a}_1] = [0 \quad \cdots \quad 0 \quad a_{\text{inc},p}^{(1)} \quad 0 \quad a_{\text{inc},s}^{(1)} \quad 0 \quad \cdots \quad 0]^T \quad (4.53)$$

$$[\mathbf{b}_1] = [b_{mnp}^{(1)} \quad \cdots \quad b_{mns}^{(1)} \quad \cdots]^T \quad (4.54)$$

$$[\mathbf{a}_2] = [a_{\text{TM},pq}^{(2)} \quad \cdots \quad a_{\text{TE},pq}^{(2)} \quad \cdots]^T \quad (4.55)$$

$$[\mathbf{b}_2] = [b_{\text{TM},pq}^{(2)} \quad \cdots \quad b_{\text{TE},pq}^{(2)} \quad \cdots]^T \quad (4.56)$$

$$[\mathbf{a}_3] = [a_{mnp}^{(3)} \quad \cdots \quad a_{mns}^{(3)} \quad \cdots]^T \quad (4.57)$$

$$[\mathbf{b}_3] = [b_{mnp}^{(3)} \quad \cdots \quad b_{mns}^{(3)} \quad \cdots]^T. \quad (4.58)$$

Thus (4.36), (4.40), (4.43), and (4.46) can be expressed as

$$[\mathbf{a}_1] + [\mathbf{b}_1] = [\mathbf{M}][\mathbf{a}_2] + [\mathbf{M}][\mathbf{E}][\mathbf{b}_2] \quad (4.59)$$

$$[\mathbf{M}]^\dagger [\mathbf{Y}_1] \{[\mathbf{a}_1] - [\mathbf{b}_1]\} = [\mathbf{Y}_2] \{[\mathbf{a}_2] - [\mathbf{E}][\mathbf{b}_2]\} \quad (4.60)$$

$$[\mathbf{a}_3] = [\mathbf{M}] \{[\mathbf{E}][\mathbf{a}_2] + [\mathbf{b}_2]\} \quad (4.61)$$

$$[\mathbf{M}]^\dagger [\mathbf{Y}_3][\mathbf{a}_3] = [\mathbf{Y}_2] \{[\mathbf{E}][\mathbf{a}_2] - [\mathbf{b}_2]\} . \quad (4.62)$$

With (4.53) being given and the four matrix equations (4.59), (4.60), (4.61) and (4.62), we can determine the four column matrices (4.54), (4.56), (4.57) and (4.58).

The last step is to calculate the transmittance of this system. Because the system is considered to be lossless, the transmittance in each region must be equal. We use Poynting's theorem to calculate the energy flux through a unit cell at a given z ,

$$J(z) = \frac{1}{2} \text{Re} \left\{ \iint_{\text{unit cell}} \hat{\mathbf{z}} \cdot [\bar{\mathbf{E}}(x, y, z) \times \bar{\mathbf{H}}^*(x, y, z)] dx dy \right\}. \quad (4.63)$$

Finally, the transmittance can be obtained by dividing $J(z)$ by incoming energy flux J_0 .

Chapter 5 *Simulation Results and Discussions*

5.1 *Preamble*

In Chapter 4, our formalism is based on rectangular (or square) Bravais lattice and rectangular (or square) lattice basis (hole) for simplicity. Therefore, in this chapter, we will compare our simulation results with measurement ones restricted only to rectangular (or square) case. The dielectric constants of the substrate will be chosen to be either $\epsilon_{Si} = 11.9$ or $\epsilon_{GaAs} = 13.7$, just for matching the measurement conditions. The real dielectric constants of substrate imply that the substrate is assumed to be lossless material. The incident light in our simulation is set to be 45° -polarized for including the two possible polarizations. Besides, let us recall the two assumptions of calculation presented in Chapter 4. The first assumption is that the metal is a perfect electric conductor, so there is no EM field penetrating into the metal and apparently no surface plasmon polariton effect is considered. This is a good assumption because in our case the light frequency is at THz regime and the skin depth of the field into the metal with good conductivity can be calculated as the following [17],

$$\delta = \sqrt{\frac{2}{\mu\sigma_1\omega}}, \quad (5.1)$$

where μ is the magnetic permeability of the metal, ω is the angular frequency, and σ_1 is the real part of conductivity which can be related to imaginary part of dielectric constant ϵ_2 by [18]

$$\sigma_1 = \frac{\omega\epsilon_2}{(4\pi)^2}. \quad (5.2)$$

Since ϵ_2 of gold is a very large value (larger than 80000) in THz regime [19], the

skin depth can be calculated to be approximately 35nm which is around 1/10000 of the incident wavelength. The second assumption is that the substrate thickness is assumed to be infinite, i.e., we don't consider the dielectric waveguide effect and interference of three layer system caused by the substrate. This also can be neglected because the accuracy Δk in our measurement is set to be large enough (say, 4 cm^{-1}) to make the interference due to substrate thickness unresolved in the spectrum. As to dielectric waveguide effect, our definition of transmittance¹ can minimize this effect.



¹ The transmittance is defined to be ratio of the transmission with 2D-metal-hole array on substrate to that without 2D-metal-hole array. In addition, because of the limit to our measurement, we only focus on zero-order transmittance.

5.2 Simulation Results Compared with Measurement Results:

EOT Phenomenon

Fig. 5.1 shows the (zero-order) transmittance spectra of both simulation and experiment results. We can see that the simulation gives a very good agreement with the measured spectrum position of peak transmittance. However, there still is discrepancy between simulation and measurement results in the magnitude of peak transmittance and linewidth, or FWHM. The reason should be that we didn't consider the loss of metal in our calculation and in practice the 2D hole array can never be ideally periodic.

In order to see the EOT phenomenon, we first define the absolute transmission efficiency [1]:

$$T_{abs} = \frac{T}{F}, \quad (5.3)$$

where T is the measured (or calculated) transmittance and F is the fraction of surface area occupied by the holes. The absolute transmission efficiencies T_{abs} are 1.4 and 1.3 for simulation and measurement results in **Fig. 5.1** respectively. T_{abs} 's being larger than 1 means that the transmitted light is more than that impinges on the holes directly. This is exactly the so-called EOT phenomenon. The peak positions occur near the lattice periodicity with consideration of substrate refraction index. Therefore we know that it is mainly the lattice periodicity of the structure that makes such EOT phenomenon. Again we have to emphasize that it is a purely geometric effect because our metal is seen as PEC. No surface plasmon polariton is considered. The absolute transmission efficiency becomes larger when we reduce the hole area, as shown in **Fig. 5.2**. In **Fig. 5.2**, we reduce the hole widths from 14um to 0.5um gradually of the 2D structure with lattice constant, $d=22\text{um}$, and fixed hole length,

$a=14\mu\text{m}$, on a substrate of dielectric constant, $\epsilon_{\text{GaAs}}=13.7$. The transmission efficiency will be very large if we let the hole area be very small. This high efficiency implies that the strength of EM field is very large inside the holes. Or we can say that the energy of light impinging on the metal surface with 2D hole array is “squeezed” into the holes. In fact, this phenomenon is similar to resonant tunneling in quantum mechanics. In the case of resonant tunneling, as shown in **Fig. 5.3**, if L_1 is equal to L_2 , namely, the system is symmetric in the direction of transmission, there will be a 100% transmission regardless of the barrier heights and barrier widths, as shown in **Fig. 5.8**. Corresponding to our 2D metal hole array case which is assumed to be symmetric in the direction of transmission (i.e., free standing film), then no matter how small the holes area is, if the incoming wave can exactly couple to an isolated state of the system, the transmission of the wave can reach 100%, as shown in **Fig. 5.4**. If the system in the transmission direction is not symmetric (i.e., metal on a GaAs substrate), the transmittance will not reach 100% anymore, but still can have a very high transmission efficiency. We can see from **Fig. 5.7** for instance. We can also see this non-100% transmission for resonant tunneling in quantum mechanics, as shown in **Fig. 5.5**. Thus in principle it is convenient to make an analogy to resonant tunneling in quantum mechanics for our EOT phenomenon. With extremely large field inside the holes, an interesting application arises. That is, we can fill some optically linear materials into the holes. Those materials inside the holes will experience a remarkably large EM field, leading to non-linear optical response.

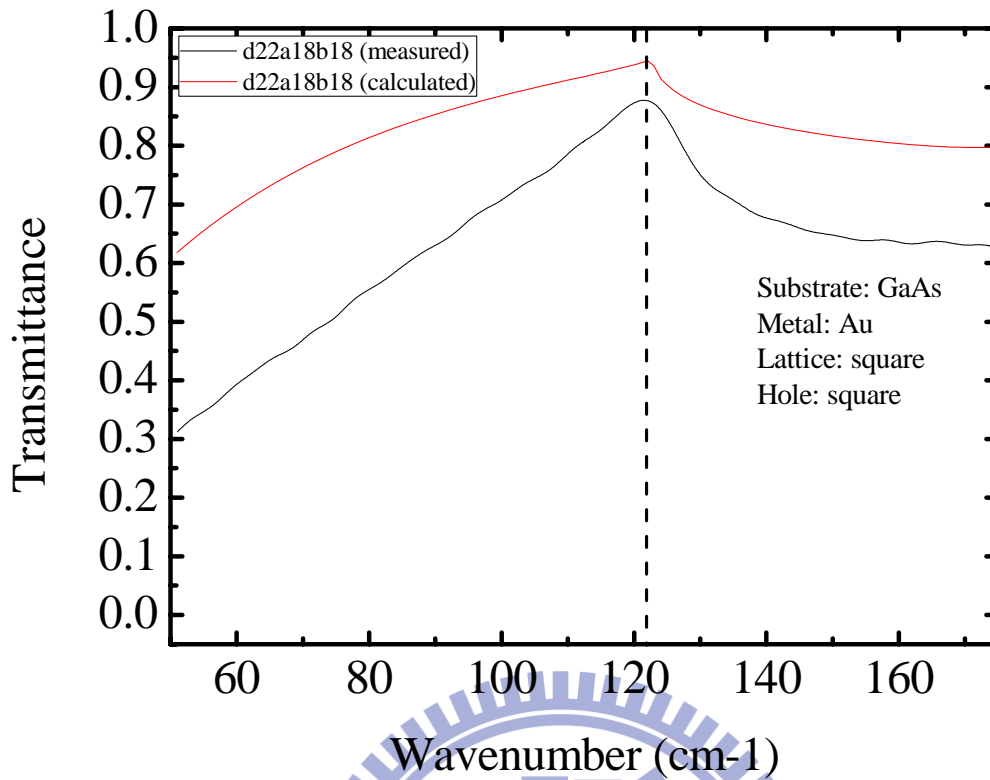


Fig. 5.1 The comparison between measured and calculated transmittance spectrum. (colors)

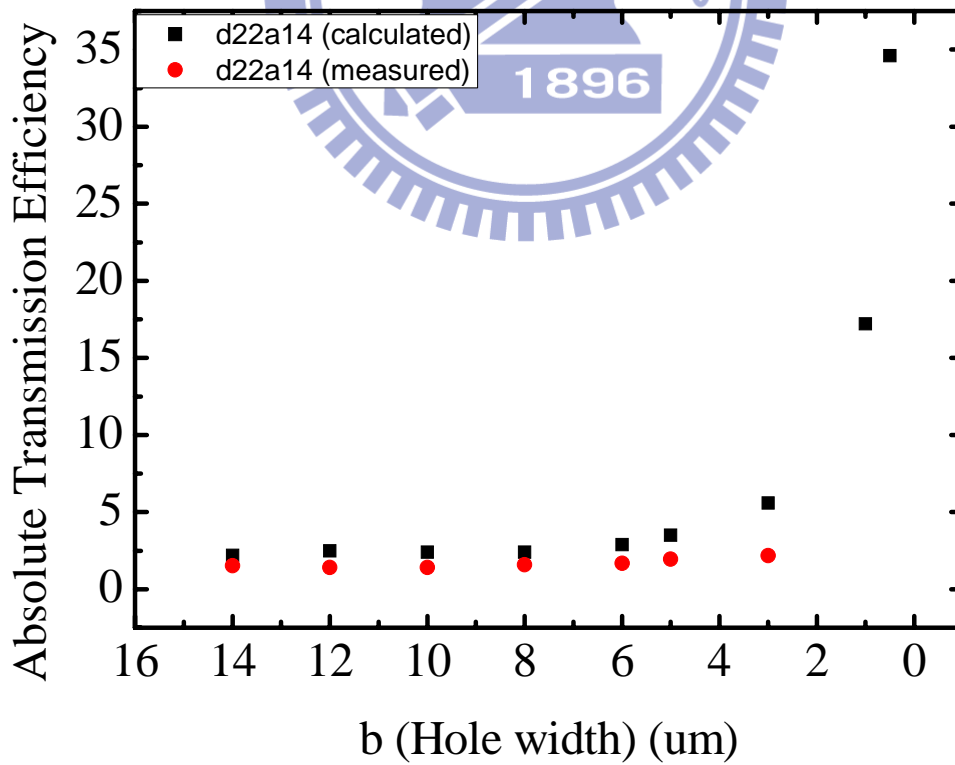


Fig. 5.2 The absolute transmission efficiencies with various holes. In this case we fix one side of the hole and vary the other side gradually.

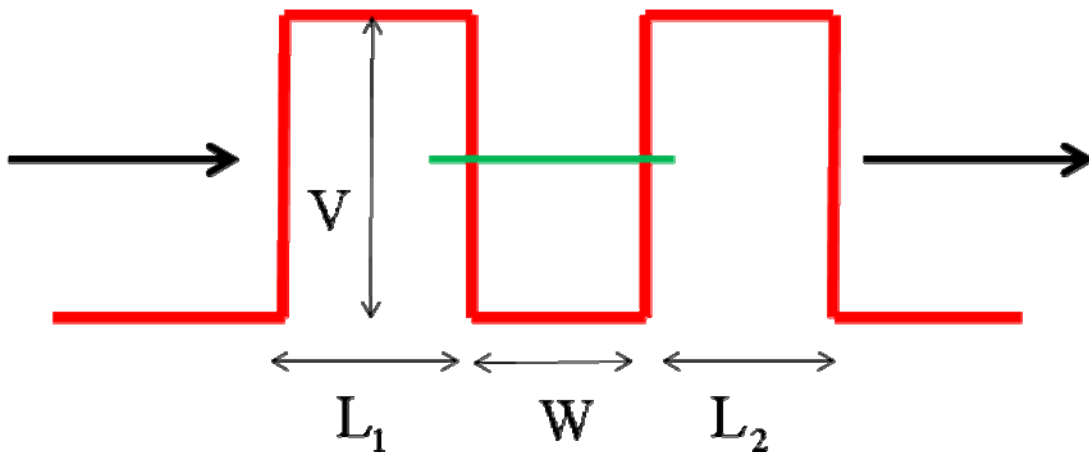


Fig. 5.3 L_1 and L_2 are the widths of the two barriers respectively. W is the width of the well. V is the barrier height.

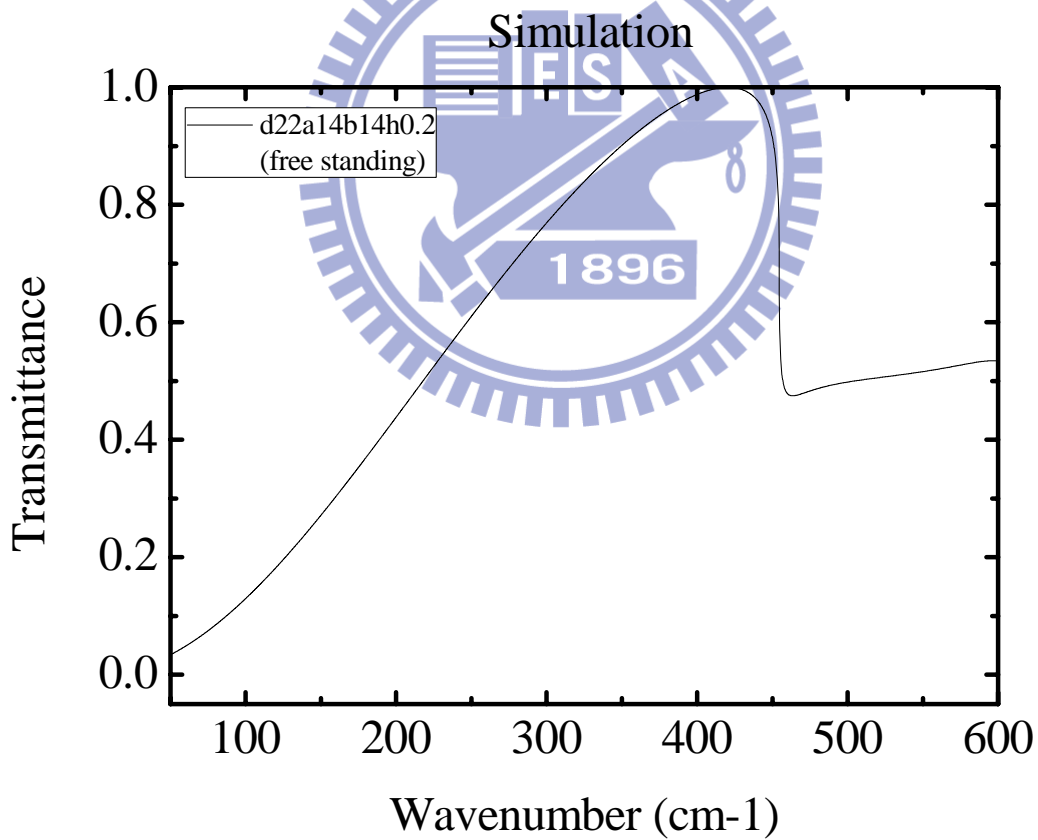
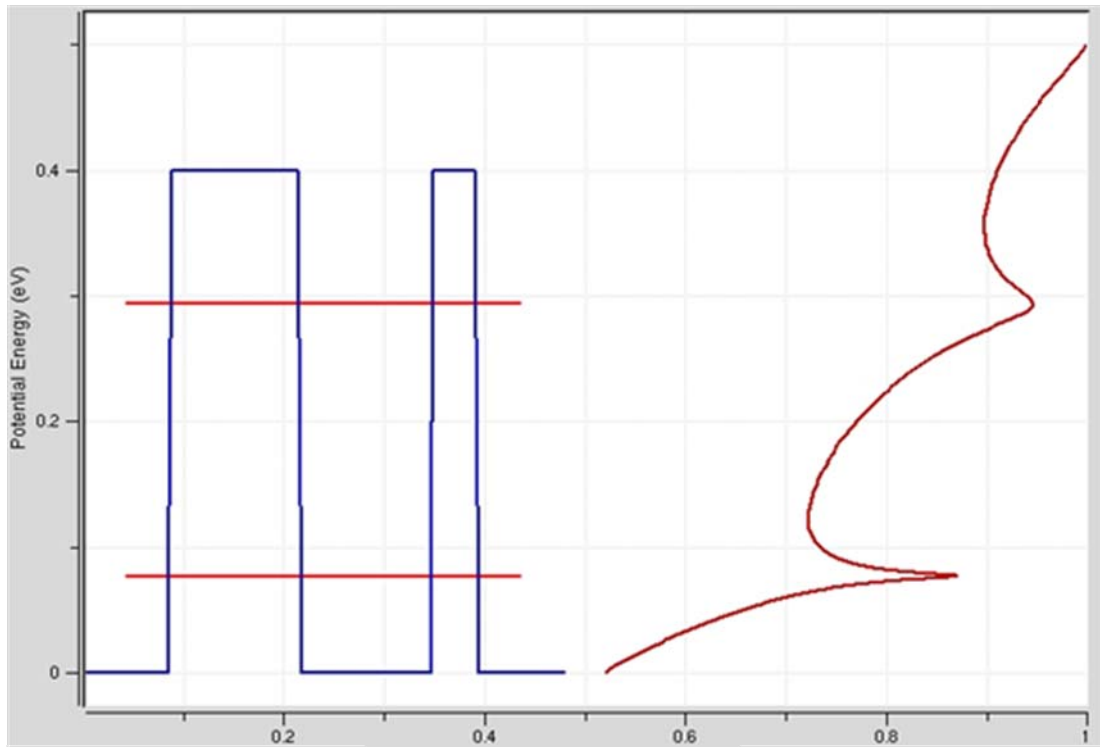


Fig. 5.4 Transmittance spectrum for free standing (the upper and lower dielectric constants are equal) case.



Transmission

Fig. 5.5 Transmission spectrum of resonant tunneling in quantum mechanics with asymmetric barriers [27].

5.3 Simulation Results Compared with Measurement Results:

Non-Monotonous Red-Shift Phenomenon

In **Fig. 3.2**, we see that the spectrum positions of peak transmittance are mostly red-shifted with increase of the aspect ratio of the holes. This red-shifted evolution has been shown and partially explained in the previous literatures [20][21][22]. While the authors in Ref. [22] attributed the red-shifted effect to the coupling between a discrete resonant state and continuum non-resonant states which is based on Fano-type resonance [23], others in Ref. [20][21] attributed the shifts to the localized resonance (or shape resonance). However, in our experiment, we found that the shift evolution is not monotonous as a function of the aspect ratio of the holes. When we continue to shrink the hole widths, i.e., to increase the aspect ratio of the holes, the peak positions eventually shift to blue. Our simulations also confirm this non-monotonous phenomenon, as shown in **Fig. 5.6(a)-(d)**. In **Fig. 5.6(a)-(d)** we can also note that there are minima occurring soon after the peaks. It is the so-called “Wood’s anomaly” of Rayleigh’s type (referred to Chapter 1). This is because that the incoming light satisfies the relation, $\sqrt{k_0^2 - |\mathbf{k}_{0//} + \mathbf{G}|^2} = 0$ and then becomes grazing to the surface, where k_0 is the incident wavevector in free space, $\mathbf{k}_{0//}$ is the in-plane component of the incident wavevector, and \mathbf{G} is the reciprocal lattice vector. Thus the spectrum positions of the minima only depend on the lattice periodicity, as can be seen in **Fig. 5.6(b)**. In 2005, F. J. Garcia, et al. derived that even a “single” hole perforated on PEC film can show a resonance near the cut-off wavelength of the hole [24]. Moreover, they made a conclusion that a rectangular hole (with aspect ratio larger than 1) will resonate “more” than a square (with aspect ratio equal to 1) or a circular hole. Consequently, a single hole on PEC can also have EOT

phenomenon. This result confirmed that there is surely a localized resonance at individual hole. In fact, the hole can be seen as an open-ended metallic low-quality-factor (low-Q) resonator [25]. This localized resonance is leakier than the discrete resonant mode caused by lattice periodicity, and it will affect the spectrum position of peak transmittance and the linewidth. In order to obtain a more physical picture, we consider this phenomenon in a simpler way. First of all, the EOT phenomenon in our case (normal incidence) is not because of a surface EM wave resonance but because of the constructive interference of evanescent wave. The reason is that our incident light is normal to the surface of the 2D structure ($\mathbf{k}_{0,z} = 0$), corresponding to the Γ point of the band structure of the system. The band structure of PEC film with 2D hole array perforated on it has been calculated by Z. Ruan and M. Qiu [25]. From the band structure in Ref. [25] we see that there are modes at the Γ point and the frequencies of those modes are very close to the spectrum position of transmission peak at normal incidence. However, what they considered is the free standing metallic film with symmetry in the z-direction while in our case the system is asymmetric (with substrate) in the z-direction. Thus it is not necessary to take into account the odd and even modes. The role of each hole can be seen as the source of evanescent field in the z-direction. Then each evanescent field forms constructive interference through the 2D periodicity. Basically the periodicity (lattice constant) determines the spectrum position of transmission peak. The hole shapes (lattice basis) will modify the band structure of the system. An apparent influence on the transmission spectrum by the holes is the linewidth. The larger the hole area, the more broadening the spectrum. This can be seen in **Fig. 5.7**. An analogy of two-barrier-one-well band structure in quantum mechanics can illustrate this idea. The transmission characteristics of such structure with different barriers are shown in **Fig.**

5.8. This is the well-known resonant tunneling in quantum mechanics. We can see that the resonant mode is leakier (wider linewidth, as in **Fig. 5.8(a)**) with narrower potential barrier. In our structure, the larger hole corresponds to narrower potential barrier while the smaller hole corresponds to wider potential barrier.

To be more detailed, we still have to distinguish the total mechanism into hole resonance and periodicity resonance. We take **Fig. 5.6** for illustrating example. Before that, in particular, one point has to be mentioned: the polarization preference. In our simulation, we found that as the hole width b (referred to **Fig. 4.1**) decreases, the transmittance will prefer the y-axis-polarized electric field of the incident light. This result is common to Ref. [21]. Therefore, as the hole width is kept shrinking, the structure shall allow only one direction (y-axis) of the polarization of incoming light eventually. This polarization-selective characteristic can be shown in **Fig. 5.9**. Therefore, the cut-off wavelength $\lambda_{\text{cut-off}}$ of a rectangular PEC waveguide is determined by its long length, a (referred to **Fig. 4.1**). In our example (**Fig. 5.6(c)**), $\lambda_{\text{cut-off}} = 28\mu\text{m}$, which is larger than the lattice constant, $d=22\mu\text{m}$. Based on Ref. [24], it is shown that the more the aspect ratio of the hole, the stronger the localized resonance (higher quality factor). Therefore, the spectrum positions of the peak transmittance will redshift with the increasing aspect ratio. Nevertheless, if the cut-off wavelength of the hole is equal to or smaller than the lattice periodicity, the peak can hardly shift, as shown in **Fig. 5.10**. Now let's go back to **Fig. 5.6**. As we continue to shrink the hole widths, the peak positions eventually shift back. In general, we know that the higher the quality factor, the lower the coupling strength. So we attribute this non-monotonous phenomenon to the decrease of the coupling strength between the plane wave mode ($|mn\sigma\rangle$) and waveguide mode ($|TE,pq\rangle$) or

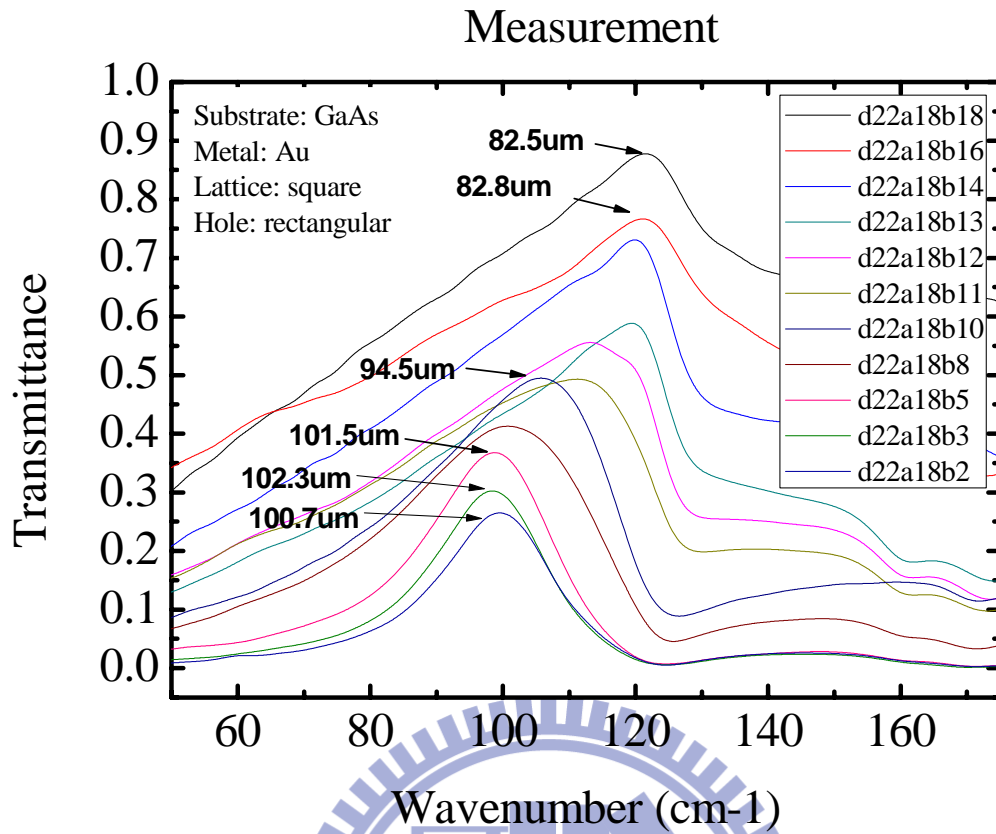


Fig. 5.6(a) Evolution of transmittance spectra with various aspect ratios. (colors)

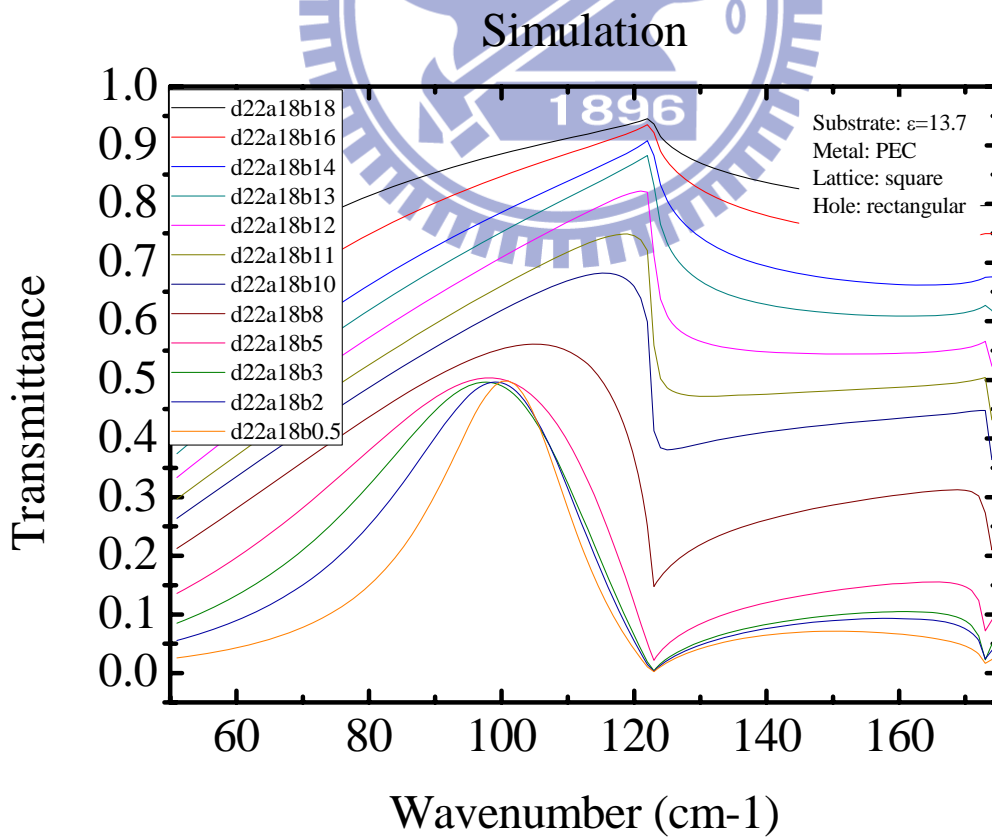


Fig. 5.6(b) Evolution of transmittance spectra with various aspect ratios. (colors)

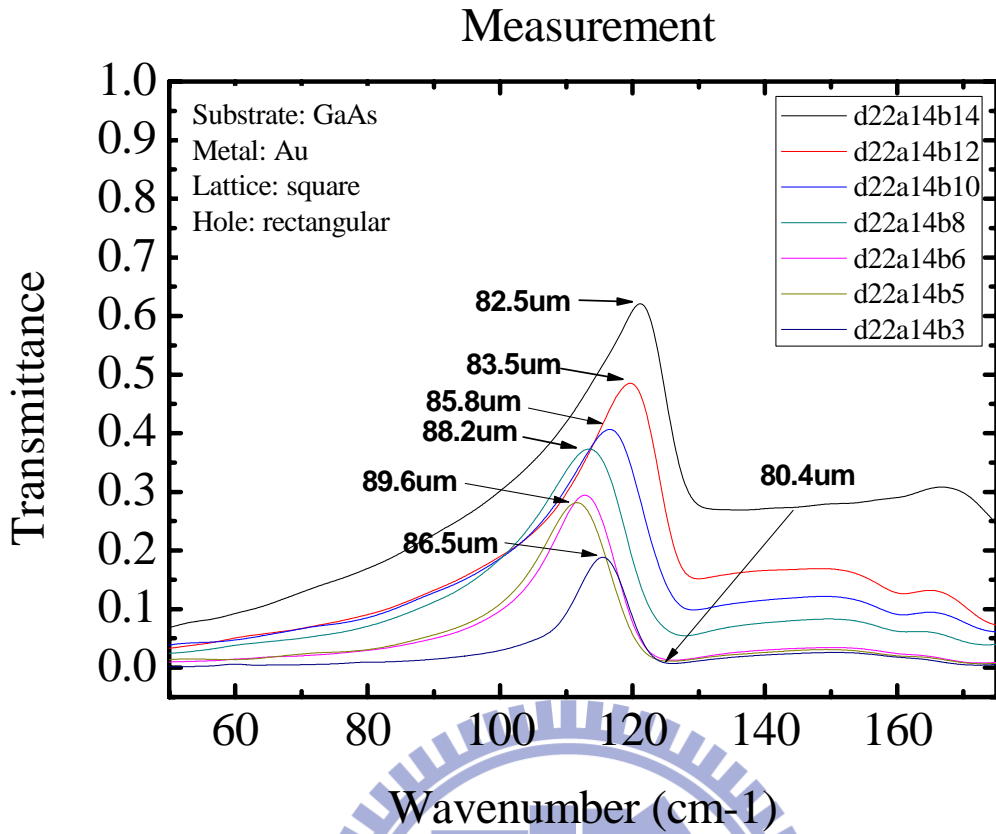


Fig. 5.6(c) Evolution of transmittance spectra with various aspect ratios. (colors)

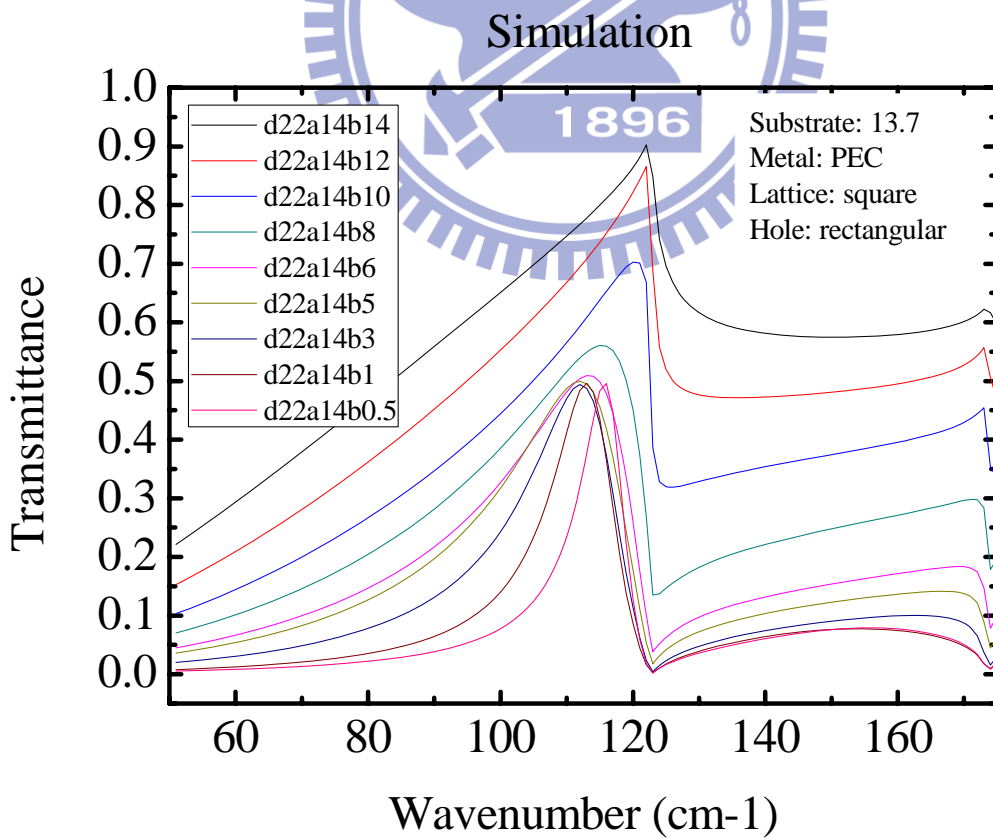
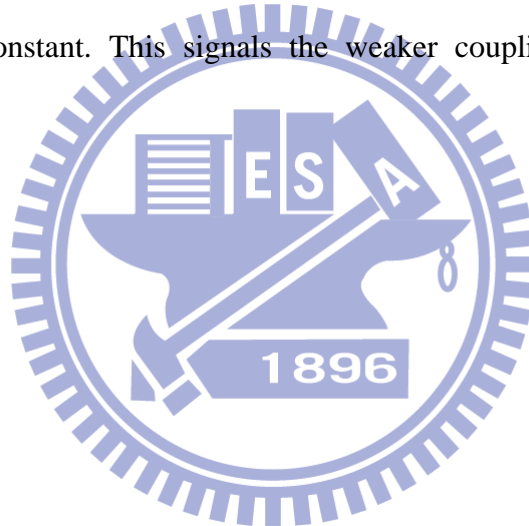


Fig. 5.6(d) Evolution of transmittance spectra with various aspect ratios. (colors)

$|TM, pq\rangle)^2$. When the coupling strength decreases to a certain degree, the influence of the hole resonance becomes minor and periodicity resonance dominates. In fact, it is hard to separate the hole resonance and periodicity resonance in this system because they are coupled together. However, we can obtain some clues when we change the lattice constant but fix the hole size and shape. As can be seen in **Fig. 5.11**, the minima of the spectra change exactly with the lattice constant while the peaks change more slowly. Notice that the labeled wavelengths have to be divided by refraction index of the substrate. Also, we can see that when the difference in dimension between the lattice constant and hole gets larger, the peaks is more indifferent to the changes of lattice constant. This signals the weaker coupling between hole and periodicity resonance.



² The detailed description of these Dirac's notations can be referred to Ch. 4.

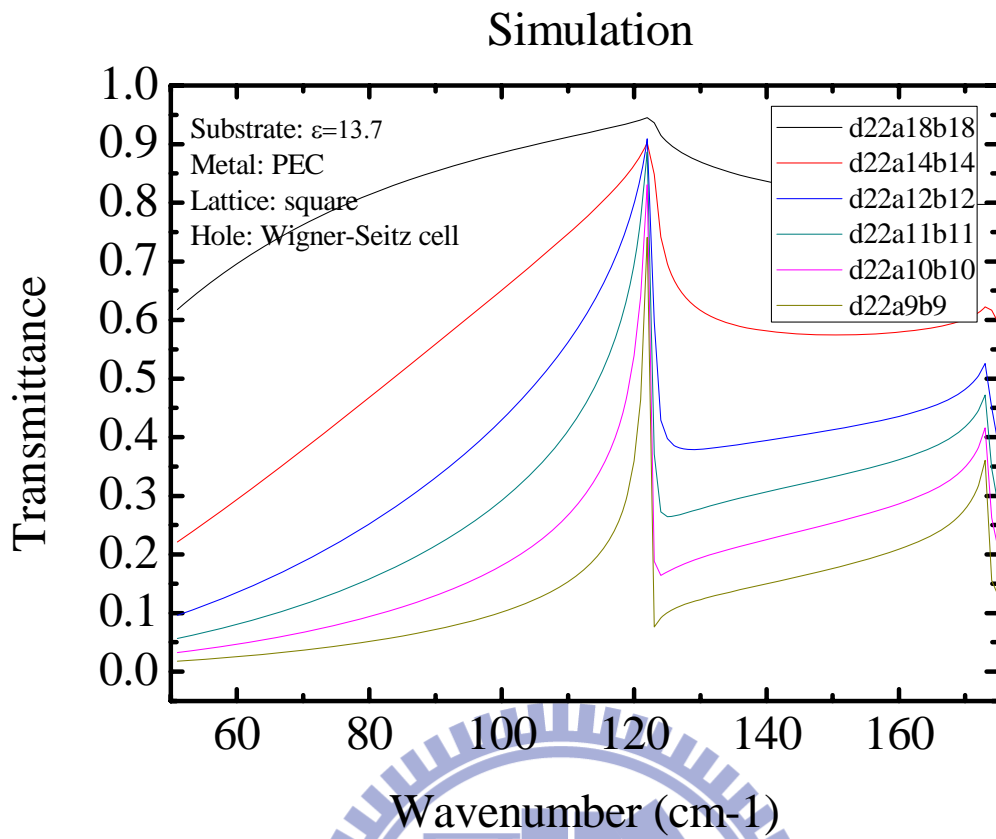
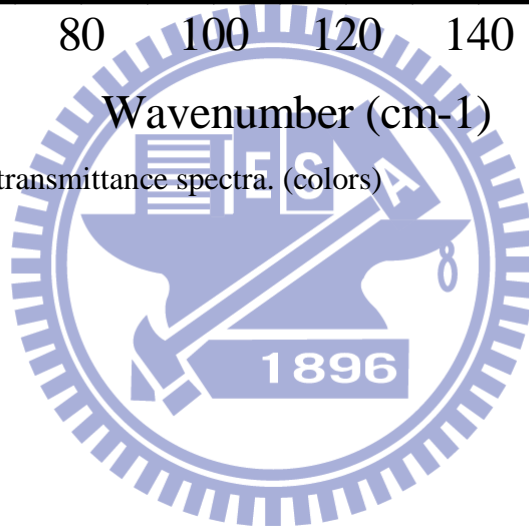


Fig. 5.7 Evolution of transmittance spectra. (colors)



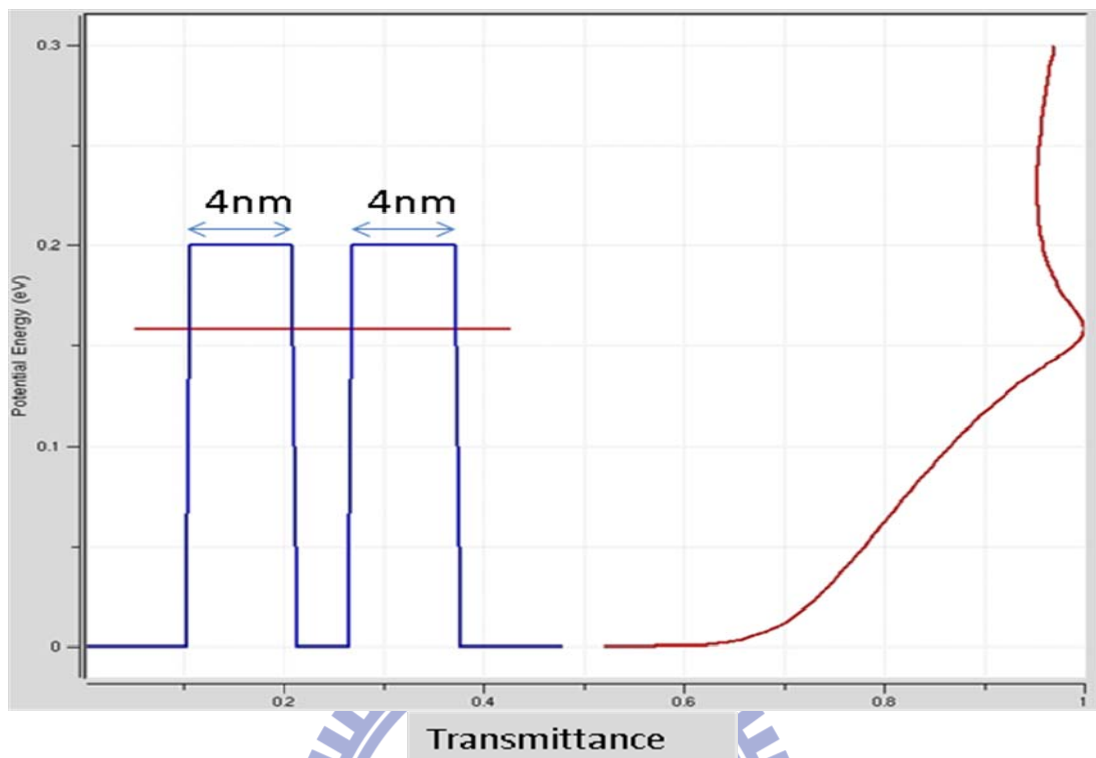


Fig. 5.8 (a) The transmission of resonant tunneling with narrower barriers [27].

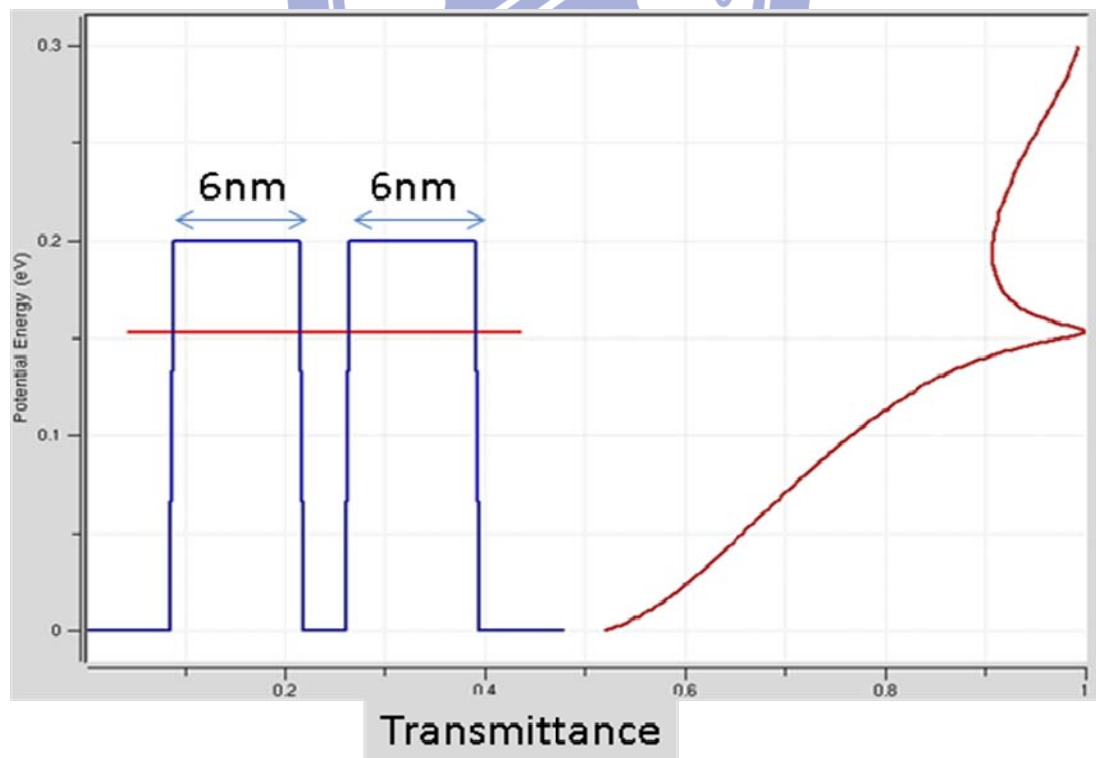


Fig. 5.8 (b) The transmission of resonant tunneling with wider barriers [27].

Simulation

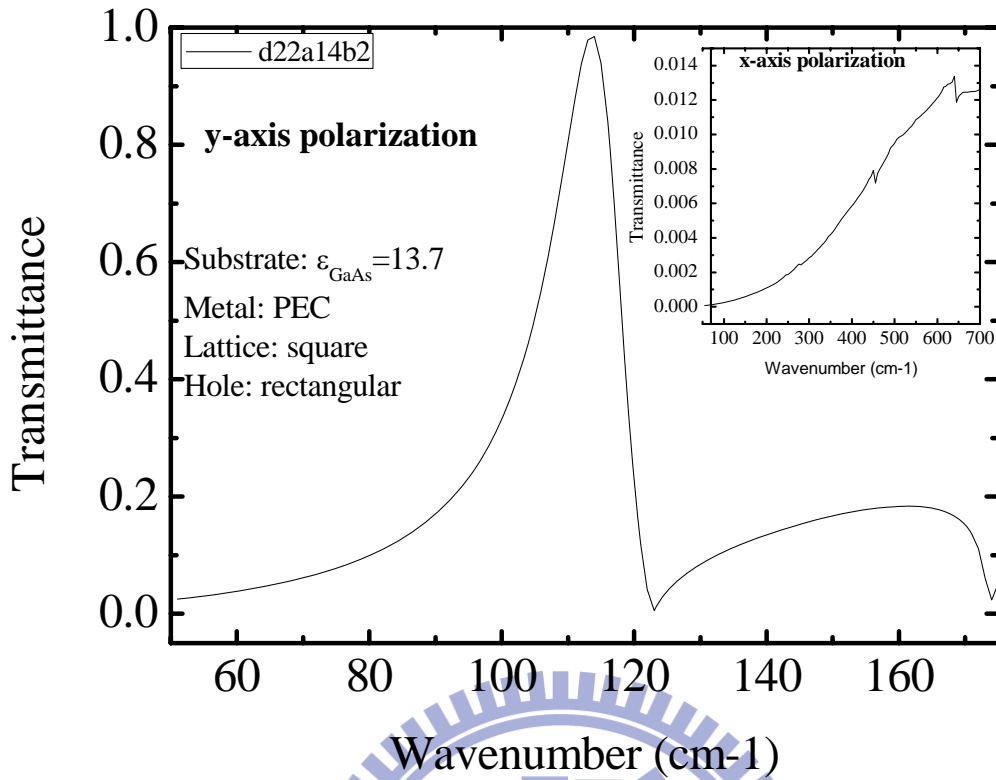


Fig. 5.9 Polarization dependence.

Simulation

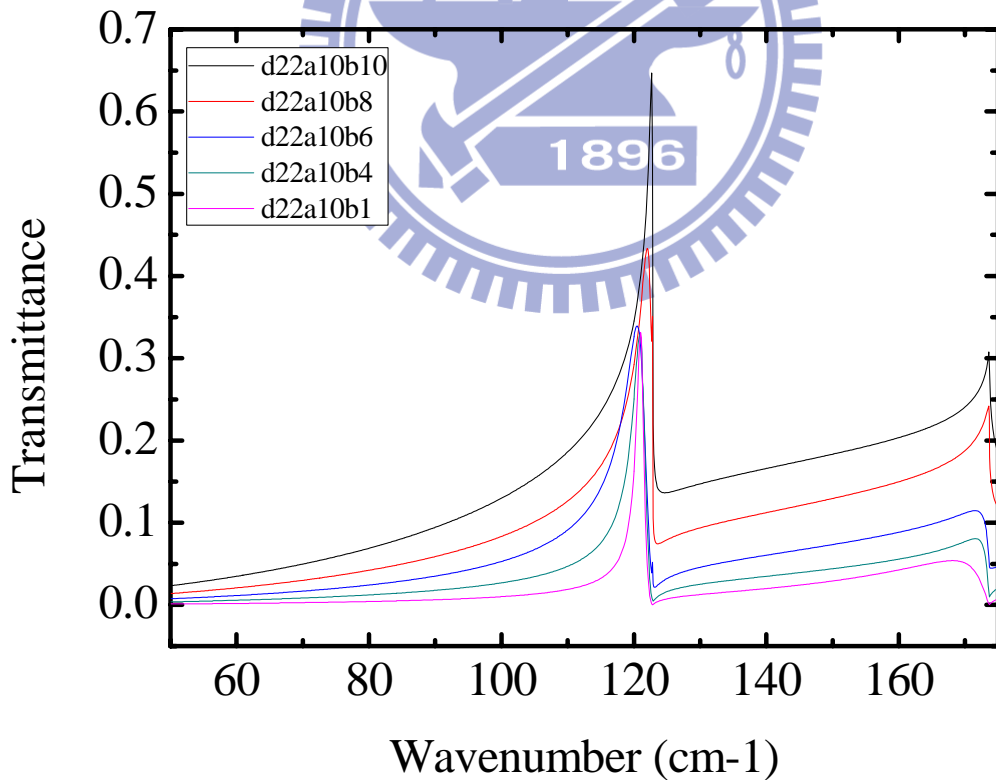


Fig. 5.10 Weak coupling strength between plane wave mode and waveguide mode. Dielectric constant of the substrate is assumed to be 13.7 (GaAs) in this simulation. (colors)

Simulation

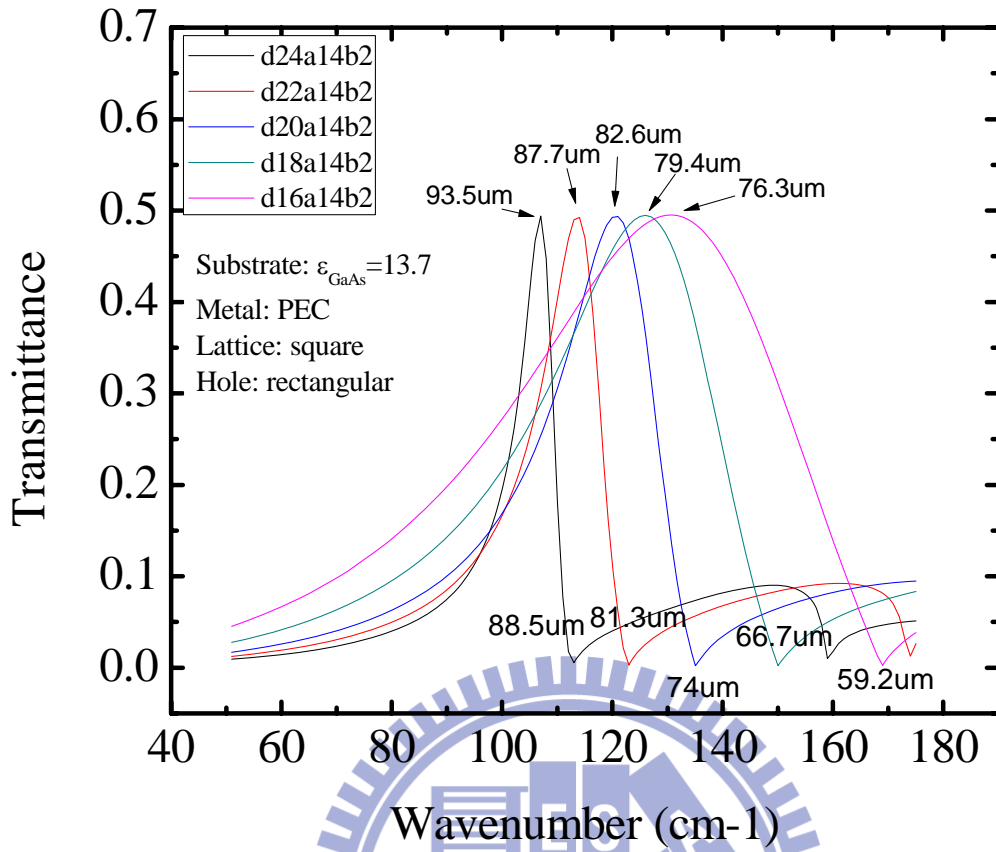


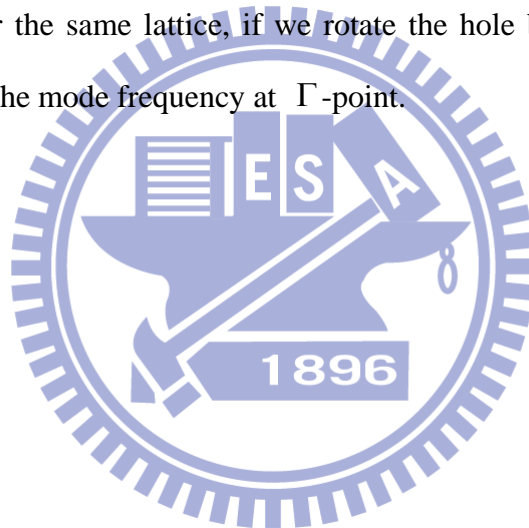
Fig. 5.11 Decoupling of the periodicity resonance and hole resonance. Dielectric constant of the substrate is assumed to be 13.7 (GaAs) in this simulation. (colors)

5.4 Simulation Results Compared with Measurement Results:

Symmetry Effect

In section 5.3, we know that the various aspect ratios of the holes can shift the peak spectrum position. However, this is not always the case. **Fig. 5.12 (a)** is an example of the holes with fixed aspect ratio 2 but various hole areas. As we can see, the spectrum position of peak transmittance does shift, and our simulation **Fig. 5.12 (b)** also confirms this result. On the other hand, if we let the hole shape be of the Wigner-Seitz cell (say, square hole) which has the same symmetry as the lattice (square lattice), the peak positions will be unchanged, as shown in **Fig. 5.13**. The magnitude difference of the peak transmittances between the measurement and simulation data is mainly due to the limited measurement resolution in wavenumber. If we enhance the wavenumber accuracy, the peak transmittance will enhance, as shown in **Fig. 5.13 (c)**. However, if we keep enhancing the wavenumber accuracy, the spectrum will be rippled because of the interference due to finite substrate thickness. Thus we have to take a trade-off. Based on the results in **Fig. 5.12** and **Fig. 5.13**, we can make a hypothesis that if the symmetry of the holes is equal or better than the symmetry of the lattice, the peak position will be fixed with various hole areas. In order to back up this hypothesis, we examined three other 2D Bravais lattices in addition to square lattice. The measurement results are shown in **Fig. 3.5**. **Fig. 5.13** shows the square lattice with square hole, **Fig. 5.14** shows the rectangular lattice (aspect ratio 2) with rectangular hole (aspect ratio 2), and **Fig. 5.15 (a)** and **Fig. 5.15 (b)** show the rectangular lattice (aspect ratio 2) with circular and square holes respectively, indicating that the peak positions are fixed when the symmetry of the hole are higher than the lattice. To explain this symmetry effect qualitatively, we calculate the eigenfrequencies of TE modes of a 2D dielectric photonic crystal by finite difference method (FDM). The general structure of unit cell of PC for

calculation is shown in **Fig. 5.16 (a)**. **Fig. 5.16 (b)** shows the eigenfrequencies distribution of two dielectric photonic crystals (PCs) with different holes but same lattice. The red dots are for the PC with the same symmetry between hole and lattice, while the blue dots are for the PC with the same hole as the red one but rotated by 90° . As we can see in **Fig. 5.14**, there is a degeneracy of eigenfrequency in the PC (red dots) with same symmetry between hole and lattice while the PC (blue dots) with different symmetry has no degeneracy. Thus we can have a physical picture that in the bandstructure of the metallic 2D hole array the one with the same symmetry between hole and lattice also has degeneracy and the mode frequency at Γ -point doesn't change. However, for the same lattice, if we rotate the hole by 90° we will lift the degeneracy and shift the mode frequency at Γ -point.



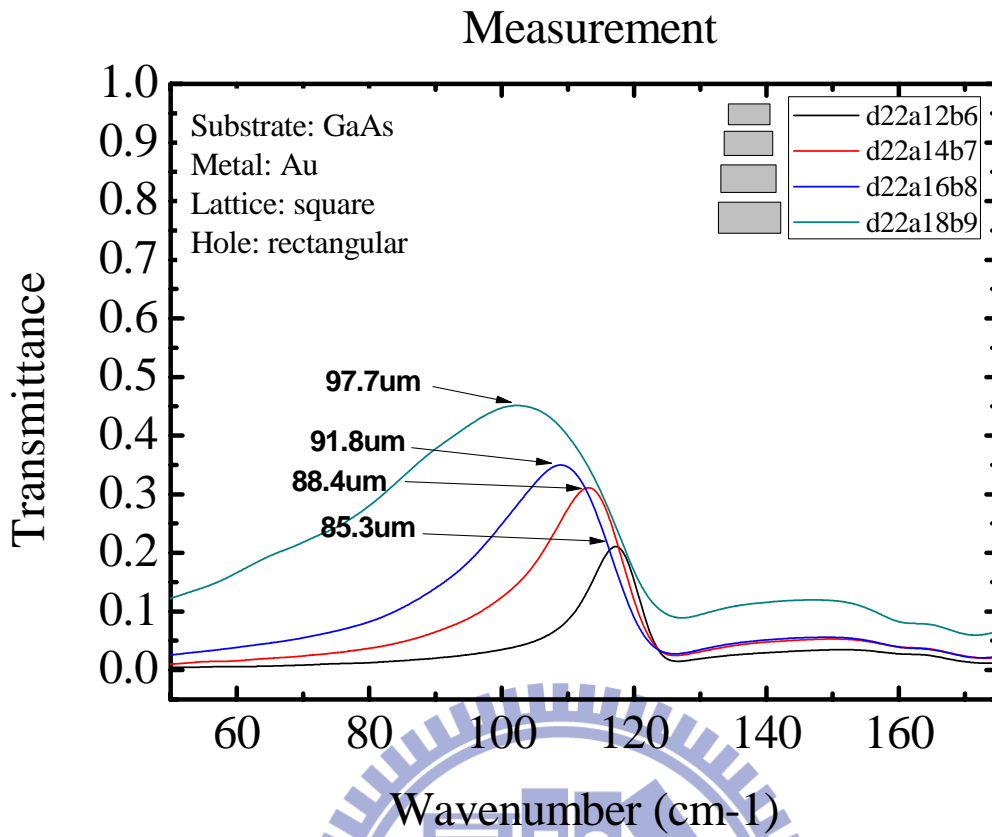


Fig. 5.12 (a) Evolution of transmission spectra. (colors)

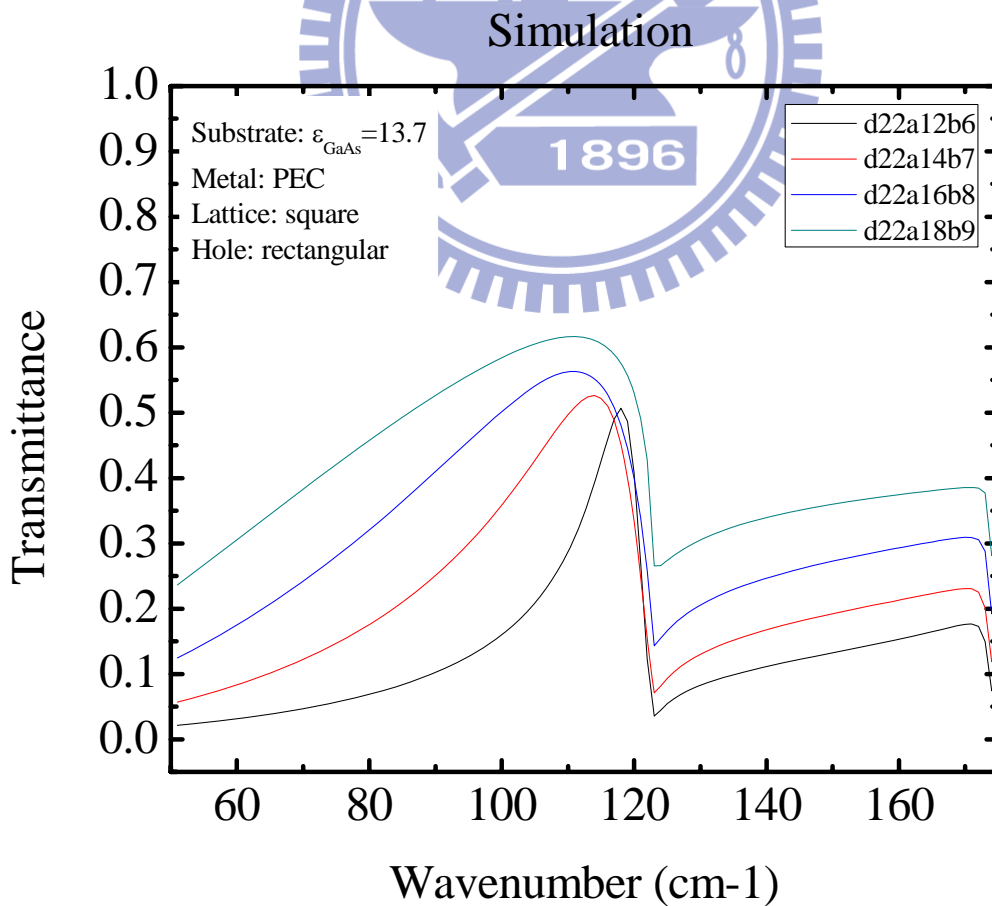


Fig. 5.12 (b) Evolution of transmission spectra. (colors)

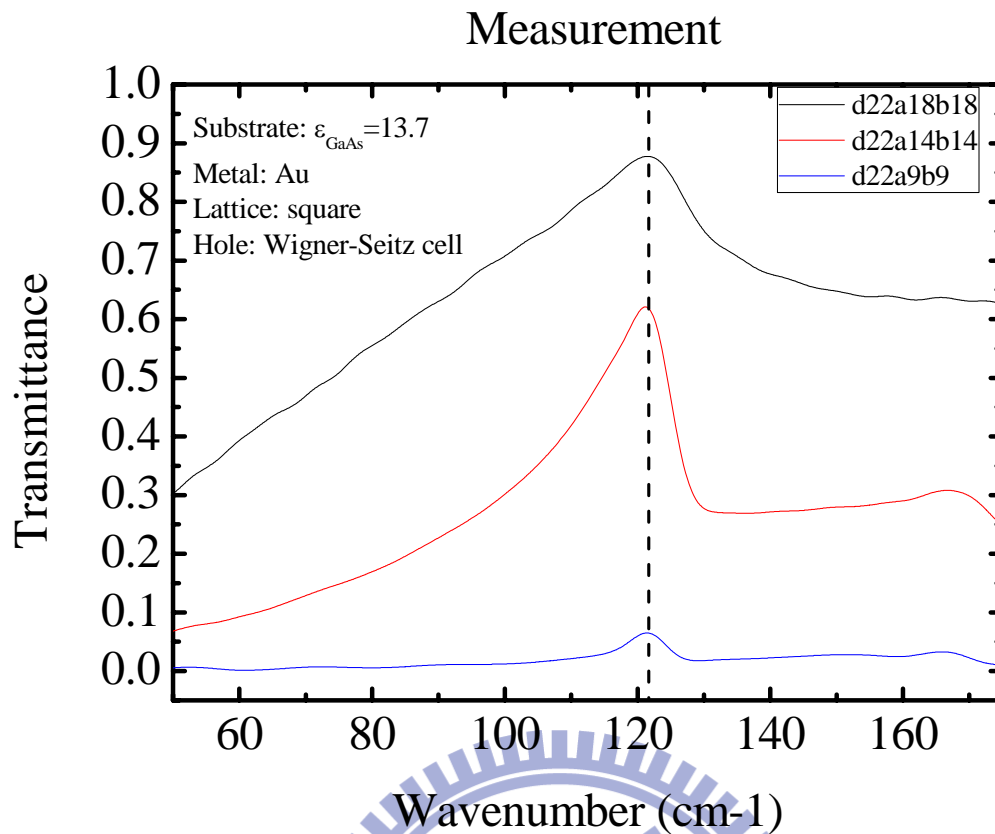


Fig. 5.13 (a) Evolution of transmission spectra. (colors)

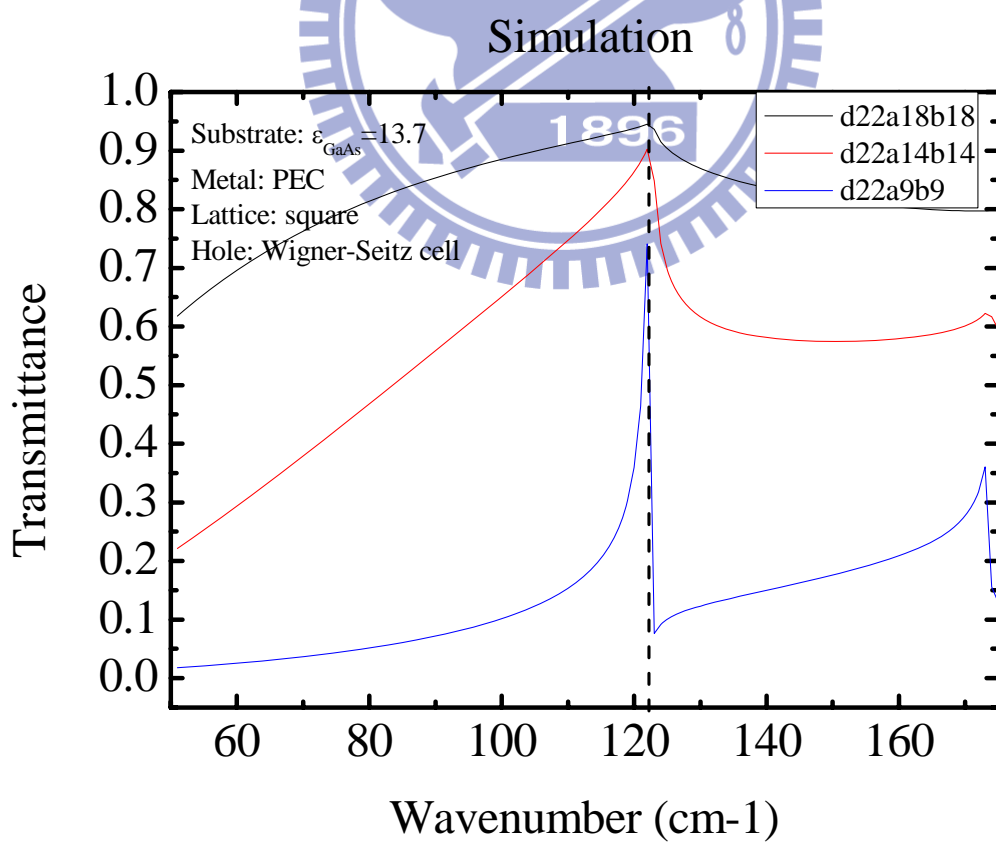


Fig. 5.13 (b) Evolution of transmission spectra. (colors)

Measurement

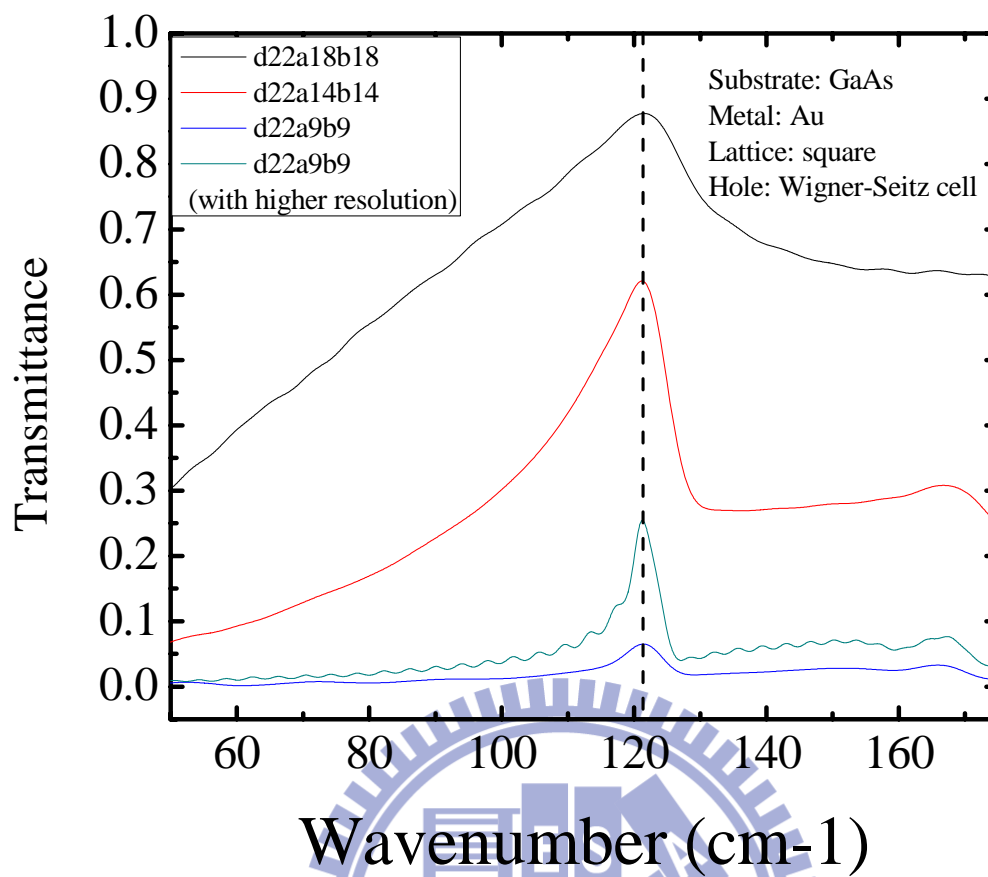


Fig. 5.13 (c) Evolution of transmission spectra. (colors)

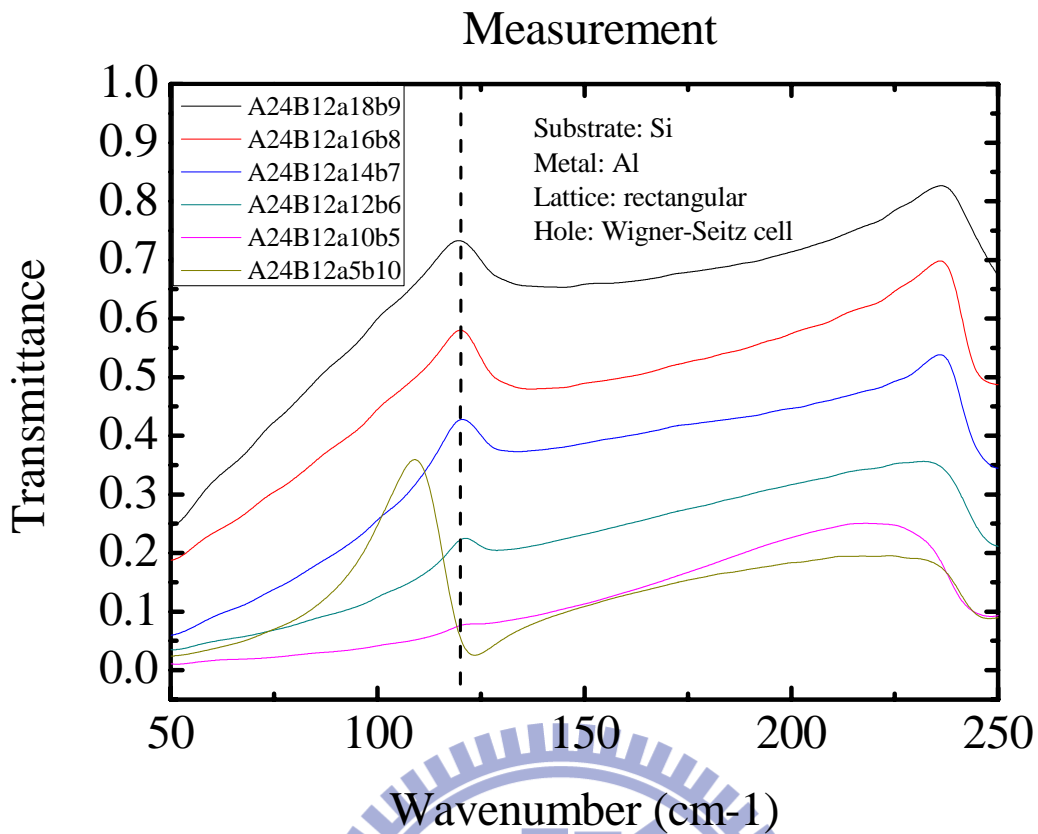


Fig.5.14 (a) Symmetry effect: evolution of transmission spectra. (colors)

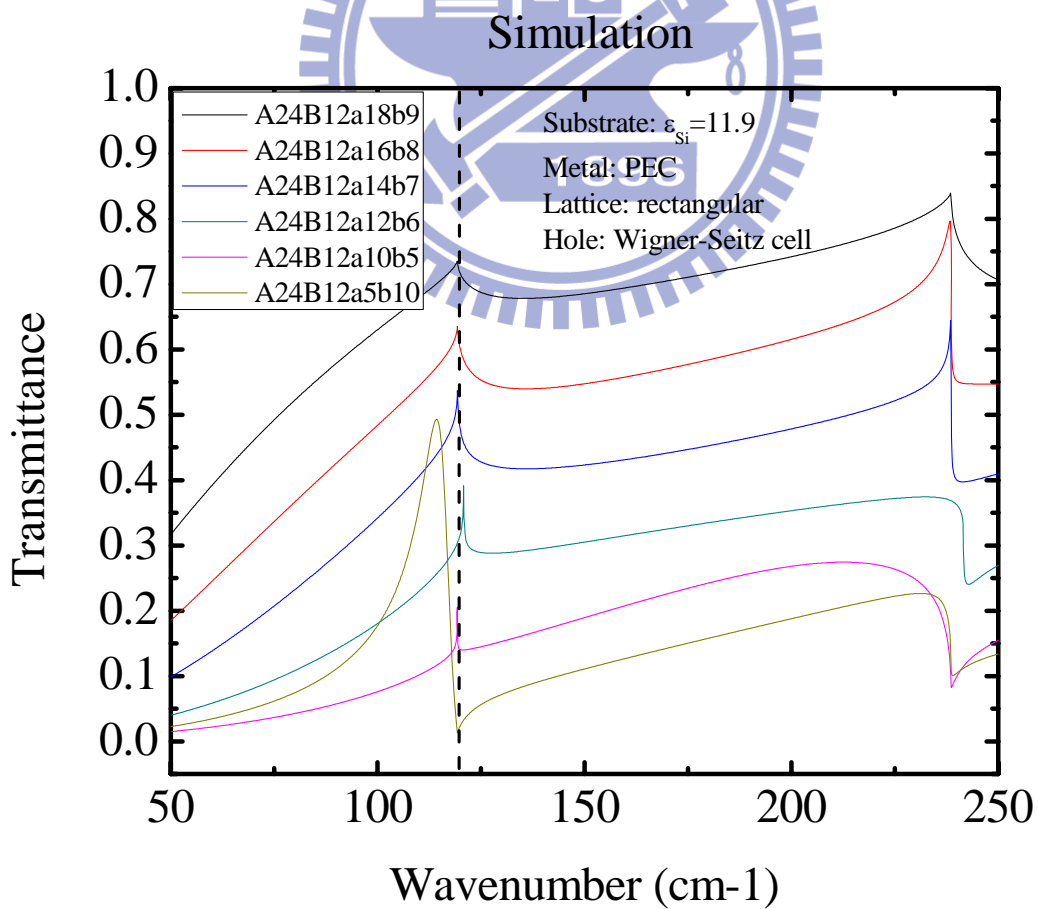


Fig. 5.14 (b) Symmetry effect: evolution of transmission spectra. (colors)

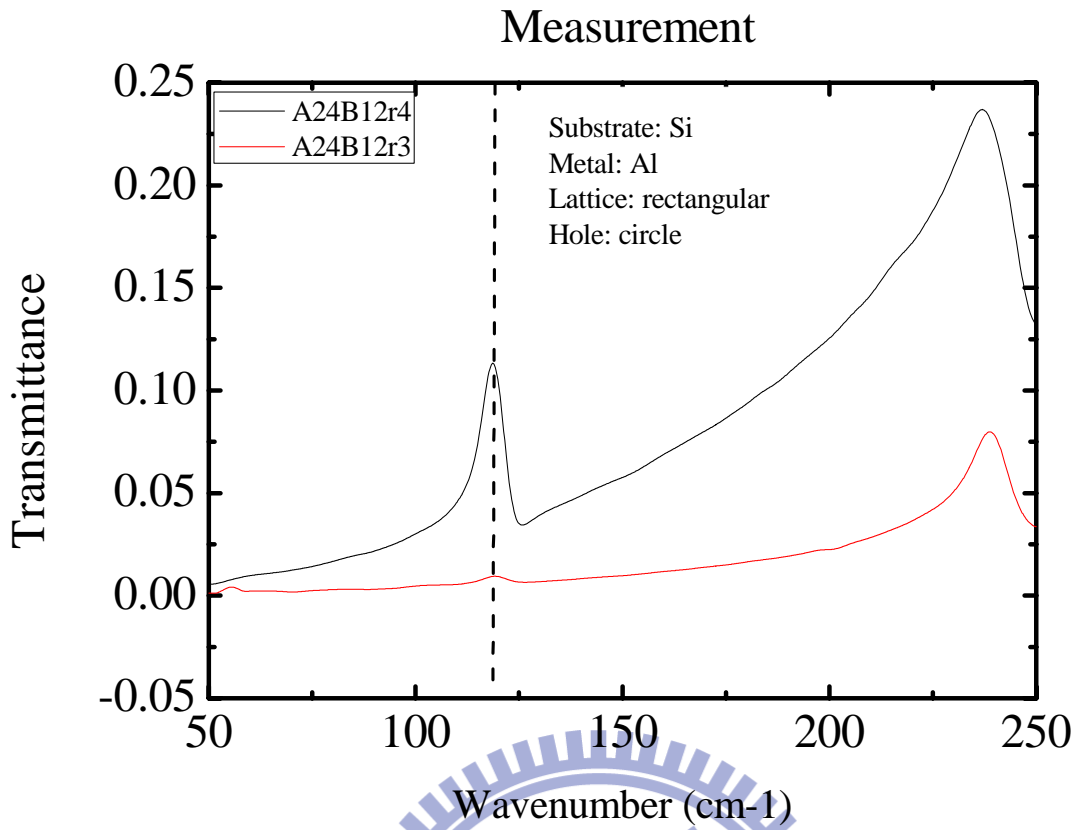


Fig. 5.15 (a) Symmetry effect: evolution of transmission spectra. The transmittance spectrum of rectangular lattice with circular basis. “r” represents the hole radius; “A” and “B” represents the lattice constant in x- and y-direction respectively. (colors)

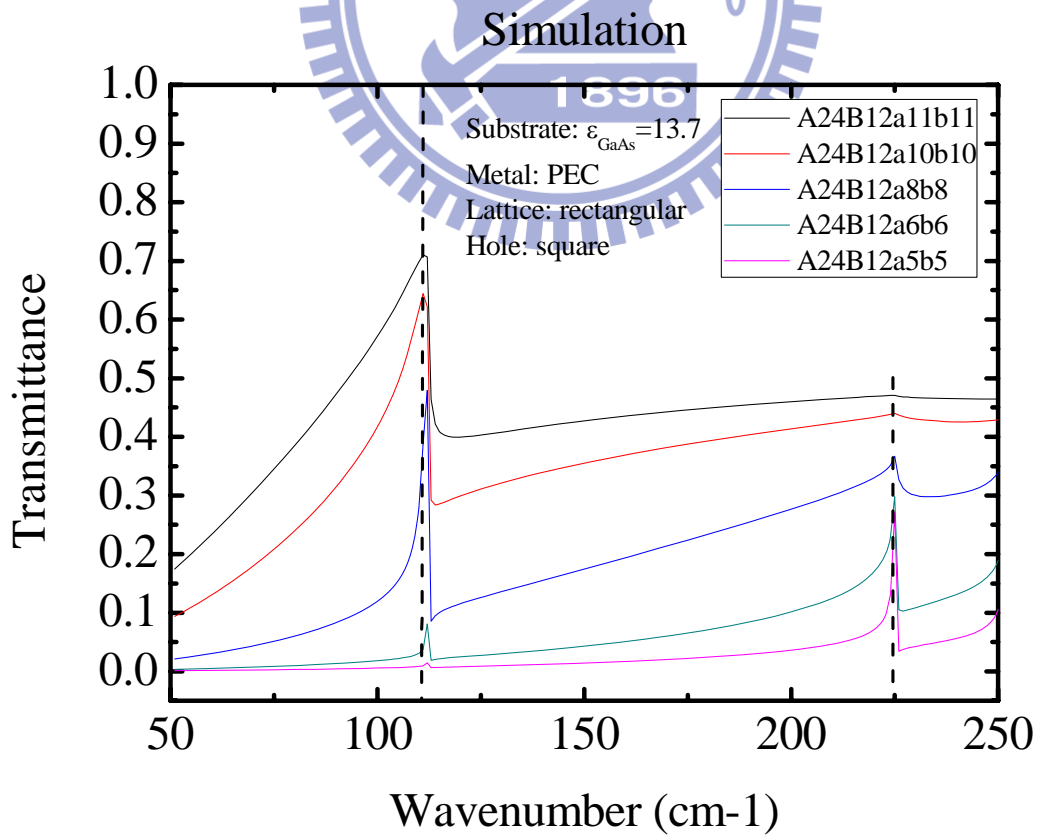


Fig. 5.15 (b) Symmetry effect: evolution of transmittance spectra. (colors)

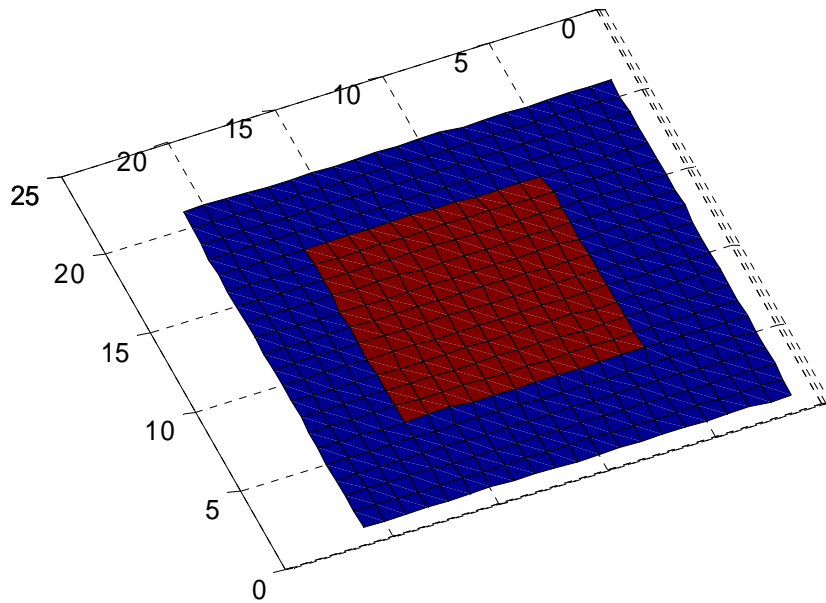


Fig. 5.16 (a) The general structure of PC for calculation of finite difference method. The blue region defines the unit cell and the dark red region defines the hole in a unit cell. (colors)

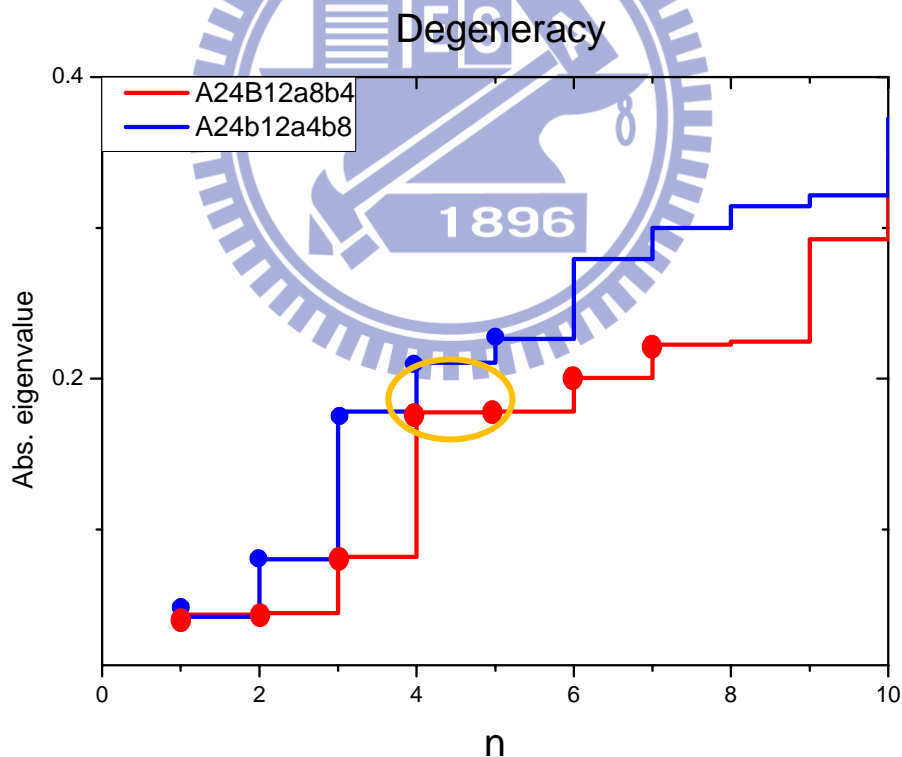


Fig. 5.16 (b) The eigenfrequency distributions of two dielectric photonic crystals with different structures. In this figure, x-axis represents the orders of eigenfrequency and y-axis represents the magnitude of eigenfrequency. The yellow circle marks the degeneracy. (colors)

Chapter 6 Conclusion

Extraordinary optical transmission (EOT) phenomenon can occur in a 2D hole array perforated on perfect electric conductor (PEC). Although there is no PEC in Nature, the PEC approximation gives a very good physical interpretation for good conductors in THz region. If the incident EM wave is normal to the surface, no surface mode is excited and the EOT phenomenon is due to constructive interference of evanescent wave caused by the subwavelength hole. Manipulating the hole shape can cause strong influence on the transmittance spectrum. If we decrease the hole area, the transmission efficiency will increase rapidly. Moreover, each hole acts as a low-Q resonator, and such resonant mode will couple with the periodicity resonant mode, and then results in shifts of the spectrum position of transmission peak. The shifts are not monotonous because the magnitude of coupling strength has to be considered. Therefore, if the hole area becomes too small, the red-shifted effect will be suppressed. We also studied the symmetry effect on transmittance spectrum. If we let the holes have the same symmetry as the lattice, i.e., let them be the Wigner-Seitz cell of the lattice, the peak position doesn't shift. In fact, the peak position will keep unchanged as long as the symmetry of the holes is equal to or better than the lattice. In this thesis, we corroborate that in THz region EOT is not due to resonantly excitation of surface plasmon polariton but due to simply the geometric effect. And the above properties of EOT phenomenon on 2D metallic hole arrays can help engineers design more elaborate THz devices.

Bibliography

1. T.W. Ebbesen, H.J. Lezec, H.F. Ghaemi, T. Thio, and P.A. Wolff, "Extraordinary optical transmission through subwavelength hole arrays", *Nature* **391**, 667, London, 1998.
2. R. W. Wood, "On a remarkable case of uneven distribution of light in a diffraction grating spectrum", *Phil. Mag.* **4**, 396, 1902.
R. W. Wood, "Anomalous diffraction gratings", *Phys. Rev.* **48**, 928, 1935.
3. Lord Rayleigh, "On the dynamical theory of gratings", *Proc. Roy. Soc. A* **79**, 399 London, 1907.
4. U. Fano, "The theory of anomalous diffraction gratings and of quasi-stationary waves on metallic surfaces (Sommerfeld's waves)", *J. Opt. Soc. Am.* **79**, 399, 1941.
5. H. Raether, *Surface Plasmons*, Vol. 111 of Springer-Verlag Tracts. in Modern Physics (Springer-Verlag, New York, 1988).
6. H.A. Bethe, "Theory of Diffraction by Small Holes", *Phys. Rev.* **66**, 163-182, 1944.
7. Martin-Moreno, et al., "Theory of Extraordinary Optical Transmission through Subwavelength Hole Arrays", *Phys. Rev. Lett.* **86**, 1114, 2001.
8. E. Popov, et al., "Theory of Light Transmission through Subwavelength Periodic Hole Arrays", *Phys. Rev. B* **62**, 16100, 2000.
9. D. E. Grupp, H. J. Lezec, T. W. Ebbesen K. M. Pellerin and Tineke Thio, "Crucial role of metal surface in enhanced transmission through subwavelength apertures", *Appl. Phys. Lett.* **77**, 1569, 2000.
10. Pendry J. B., Martin-Moreno L. and Garcia-Vidal F. J., "Mimicking Surface Plasmons with Structured Surfaces", *Science* **305**, 847, 2004.
11. F. J. Garcia-Vidal, L. Martin-Moreno and J. B. Pendry, "Surface with holes in them: new plasmonic metamaterials", *J. Opt. A: Pure Appl. Opt.* **7**, S97, 2005.
12. L. Martin-Moreno and F. J. Garcia-Vidal, "Optical transmission through circular hole arrays in optically thick metal films", *Opt. Exp.* **12**, 3619, 2004.
13. E. Moreno, et al., "Resonant Transmission of Cold Atoms through Subwavelength Apertures", *Phys. Rev. Lett.* **95**, 170406, 2005.
14. Bo Hou, et al., "Tuning Fabry-Perot resonances via diffraction evanescent waves", *Phys. Rev. B* **76**, 054303, 2007.
15. J. Christensen, et al., "Collimation of sound assisted by acoustic surface waves", *Nat. Phys.* **3**, 851, 2007.
16. L. Martin-Moreno and F. J. Garcia-Vidal, "Minimal model for optical transmission through holey metal films", *J. Phys.: Condens. Matter* **20**, 304214,

2008.

17. J. D. Jackson, Classical Electrodynamics, 3rd ed., John Wiley, U.S., 1999.
18. M. Dressel and G. Gruner, Electrodynamics of Solids: Optical Properties of Electrons in Matter, Cambridge University Press, New York, 2002.
19. M. A. Ordal, et al., “Optical Properties of the Metals Al, Co, Cu, Au, Fe, Pb, Ni, Pd, Pt, Ag, Ti, and W in the infrared and far infrared”, *s Appl. Opt.*, **22**, 1009, 1983.
20. K. L. van der Molen, et al., “Role of Shape and Localized Resonances in Extraordinary Transmission through Periodic Arrays of Subwavelength Holes: Experiment and Theory”, *Phys. Rev. B* **72**, 045421, 2005.
21. K. J. Klein Koerkamp, et al., “Strong Influence of Hole Shape on Extraordinary Transmission through Periodic Arrays of Subwavelength Holes”, *Phys. Rev. Lett.* **92**, 183901, 2004.
22. J. Han, et al., “Coupling between Surface Plasmons and Nonresonant Transmission in Subwavelength Holes at Terahertz Frequencies”, *Appl. Phys. Lett.* **91**, 071122, 2007.
23. U. Fano, “Effect of Configuration Interaction on Intensities and Phase Shifts”, *Phys. Rev.* **123**, 1866, 1961.
24. F. J. Garcia-Vidal, et al., “Transmission of Light through a Single Rectangular Hole”, *Phys. Rev. Lett.* **95**, 103901, 2005.
25. Z. Ruan and M. Qiu, “Enhanced Transmission through Periodic Arrays of Subwavelength Holes: The Role of Localized Waveguide Resonances”, *Phys. Rev. Lett.* **96**, 233901, 2006.
26. R. Gordon and A. G. Brolo, “Increased cut-off wavelength for a subwavelength hole in a real metal”, *Opt. Exp.* **13**, 1933, 2005.
27. <http://www.nanohub.org/>

Autobiography (自傳)

姓名：黃品維 (Huang, Pin-Wei)

性別：男

出生年月日：民國 73 年 8 月 20 日

學歷：

國立交通大學電子工程學系 (92.9 - 96.6)

國立交通大學電子工程研究所碩士班 (96.9 - 98.6)

碩士論文題目：

異常光學穿透現象於兆赫波段之研究

Study of Extraordinary Optical Transmission in THz Region

